Research Square

Preprints are preliminary reports that have not undergone peer review.
They should not be considered conclusive, used to inform clinical practice,
or referenced by the media as validated information.

Interfacial and Electronic-Structure Control of Multi-Electron CO2 Reduction for Solar Liquid Fuel Production

Young Soo Kang

yskang@kentech.ac.kr

Korea Institute of Energy Technology (KENTECH) https://orcid.org/0000-0001-5746-8171

Ramesh Poonchi Sivasankaran

Korea Institute of Energy Technology (KENTECH)

Stephanie Restu Pratiwi Sutjijana

Sogang University

Amol Pawar

KENTECH

Sampath Prabhakaran

Korea Institute of Ceramic Engineering and Technology https://orcid.org/0000-0003-1568-7864

Sunmoon Yu

Massachusetts Institute of Technology

Long Yang

Southwest University of Science and Technology https://orcid.org/0000-0001-5554-5209

Lee Don Keun

KENTECH

Kyoung Mo Park

Korea Institute of Energy Technology (KENTECH)

Min Seong Kim

Korea Institute of Energy Technology (KENTECH)

Hyunchul Shin

EST Energy

Do Hwan Kim

Jeonbuk National University https://orcid.org/0000-0002-2976-6873

Hongxian Han

Dalian Institute of Chemical Physics https://orcid.org/0000-0002-2522-1817

Yang Shao-Horn

Massachusetts Institute of Technology https://orcid.org/0000-0001-8714-2121

Article

Keywords:

Posted Date: June 9th, 2026

DOI: https://doi.org/10.21203/rs.3.rs-8375410/v1

License: This work is licensed under a Creative Commons Attribution 4.0 International License.
Read Full License

Additional Declarations: There is **NO** Competing Interest.

Interfacial and Electronic-Structure Control of Multi-Electron CO_2 Reduction for Solar Liquid Fuel Production

Ramesh Poonchi Sivasankaran[1], Stephanie Restu Pratiwi Sutjijana[2], Amol Uttam Pawar[1], Sampath Prabhakaran[3,4], Sunmoon Yu[5], Long Yang[1], Don Keun Lee[1], Kyoung Mo Park[1], Min Seong Kim[1], Hyunchul Shin[6], Do Hwan Kim[4], Hongxian Han[7], Yang Shao-Horn[5,8], and Young Soo Kang[1,*]

[1]Carbon Resources Conversion Research Center, School of Energy Engineering, Korea Institute of Energy Technology (KENTECH), 21 Kentech-gil, Naju 58330, Republic of Korea.

[2]Department of Chemistry, Sogang University, #1 Shinsu-dong, Mapo-gu, Seoul 121-742, Republic of Korea.

[3]Division of AI convergence Research, Korea Institute of Ceramic Engineering and Technology (KICET), Jinju, 52851, Republic of Korea

[4]Division of Science Education, Department of Energy Storage/Conversion Engineering (BK21 FOUR), Jeonbuk National University, Jeonju, Jeonbuk, 54896, Republic of Korea.

[5]Research Laboratory of Electronics, Massachusetts Institute of Technology, Cambridge, Massachusetts 02139, United States.

[6]EST Energy, Jinsun building, 28, Takeunosaneop-ro 81 beon-gil, Nam-gu, Ulsan 44776, Republic of Korea.

[7]State Key Laboratory of Catalysis, Dalian Institute of Chemical Physics, Chinese Academy of Sciences, Dalian National Laboratory for Clean Energy, Dalian,116023, P. R. China.

[8]Department of Materials Science and Engineering, Department of Mechanical Engineering, and Department of Chemistry, Massachusetts Institute of Technology, Cambridge, Massachusetts 02139, United States.

*** Corresponding author**: Young Soo Kang (yskang@kentech.ac.kr)

Understanding and controlling the multi-electron reduction of CO_2 with molecular-level precision remains a fundamental challenge in developing chemical routes for solar liquid fuel production. Here, we present an interfacially engineered strategy that couples a single-crystalline (040)-faceted $BiVO_4$ photoanode with a $Cu/Cu_{10}Sn_3$/poly(4-vinylpyridine)/reduced graphene oxide/Nafion multi-layer cathode to enable selective photoelectrochemical CO_2 reduction into solar liquid fuels. The multi-layer dark cathode strategically integrates, $Cu_{10}Sn_3$ alloy nanoparticles to accelerate electron transfer, rGO to mediate sequential multi-electron shuttling, poly(4-vinylpyridine) to promote CO_2 capture and activation, and a Nafion overlayer to facilitate rapid proton transport to the CO_2 reduction sites. *In-situ* Raman, ATR-IR, and EPR spectroscopy reveal the sequential formation of $CO_2^{\bullet-}$, *OCHO, COOH*, *CO*, and *CO–CO* reaction intermediates that steer product selectivity toward methanol, ethanol, and formaldehyde with a total Faradaic efficiency of ~91.8% and a solar-to-fuel efficiency of ~1.78%. Complementary density-functional-theory calculations corroborate the energetics and electronic-structure evolution of these intermediates, providing mechanistic insight into interfacial charge transfer and C–C coupling. Together, these findings establish a mechanistic framework for directing CO_2 activation through interfacial and electronic-structure control, offering chemically generalizable principles for solar-driven fuel generation.

Artificial photosynthesis is an attractive strategy for producing solar liquid fuels by enabling efficient solar energy conversion.[1,2] Specifically, it facilitates the CO_2 reduction reaction (CO_2RR) by mimicking natural photosynthesis to generate solar liquid fuels, including methanol, ethanol and formaldehyde *via* different transport pathways of sequential multi-proton/multi-electron transfer.[3,4] Among various strategies, photoelectrochemical CO_2RR (PEC CO_2RR) is the most promising method for producing solar liquid fuels, as it can mitigate the high input energy and process cost of the electrochemical CO_2RR and the low product selectivity of the photocatalytic CO_2RR.[5,6] Copper-based dark cathodes are extensively studied for CO_2RR due to their ability to produce multi-carbon products, but they often suffer from poor selectivity.[7,8] To address this issue, Cu-based bimetallic alloy catalysts have gained significant attention for enhancing CO_2RR activity and selectivity through synergistic effects and intermediate stabilization.[9] Various bimetallic alloy catalysts, including Cu-Ni,[10,11] Cu-Zn,[12,13] Cu-In,[14,15] Cu-Sn,[9,16,17] Cu-Ag,[18,19] Cu-Au[20,21] and Cu-Pd[22,23] have been reported to exhibit enhanced CO_2RR activity and selectivity. Among them, Cu-Sn alloys are particularly promising due to their high charge capacity and electronic conductivity.[9,16,17] However, Cu-Sn alloys still exhibit limited performance in solar liquid fuel production due to their insufficient ability to accumulate multiple electrons for facilitating sequential multi-electron/multi-proton transfer through different transport pathway, as well as their poor suppression of the competing hydrogen evolution reaction (HER).[17]

Reduced graphene oxide (rGO) is considered as a promising carbon-based polymeric material for its unique sequential multi-electron transfer function due to its large charge capacity and optimal electronic conductivity.[6,24,25] In the hybrid CuSn alloy/rGO system, electron transfer from the CuSn alloy to rGO occurs through a non-Faradaic process, enabling substantial electron accumulation owing to the large charge-storage capacity and excellent electronic conductivity of rGO[6,24,26,27] These unique properties facilitate efficient electron transfer from rGO to CO_2 reduction sites, promoting solar liquid fuel production through sequential multi-electron transfer processes. Poly(4-vinyl)pyridine (PVP) contains N-heterocyclic pyridinium functional groups, which plays a crucial role in efficiently capturing and activating CO_2 molecules by forming a [$PVP^{\delta+}$-$CO_2^{\delta-}$] complex, thereby raising the energy level of the reactant state and lowering the transition-state energy

barrier.[28,29] The partially deprotonated pyridine sites under optimal pH further promote CO_2 capturing and activation. Additionally, PVP plays a crucial role in enhancing the efficiency of CO_2RR due to its hydrophobic nature, which facilitates the adsorption of hydrophobic CO_2 molecules onto its surface. Consequently, this hydrophobic property of PVP leads to an extended adsorption lifetime for CO_2 molecules and intermediates, thereby increasing the lifetime for accepting sequential multi-electrons/multi-protons.[28,29] This extended adsorption lifetime enhances the probability of sequential electron and proton transfer, thereby accelerating the overall reaction kinetics and improving product selectivity, ultimately driving the CO_2RR process toward the efficient production of solar liquid fuels.

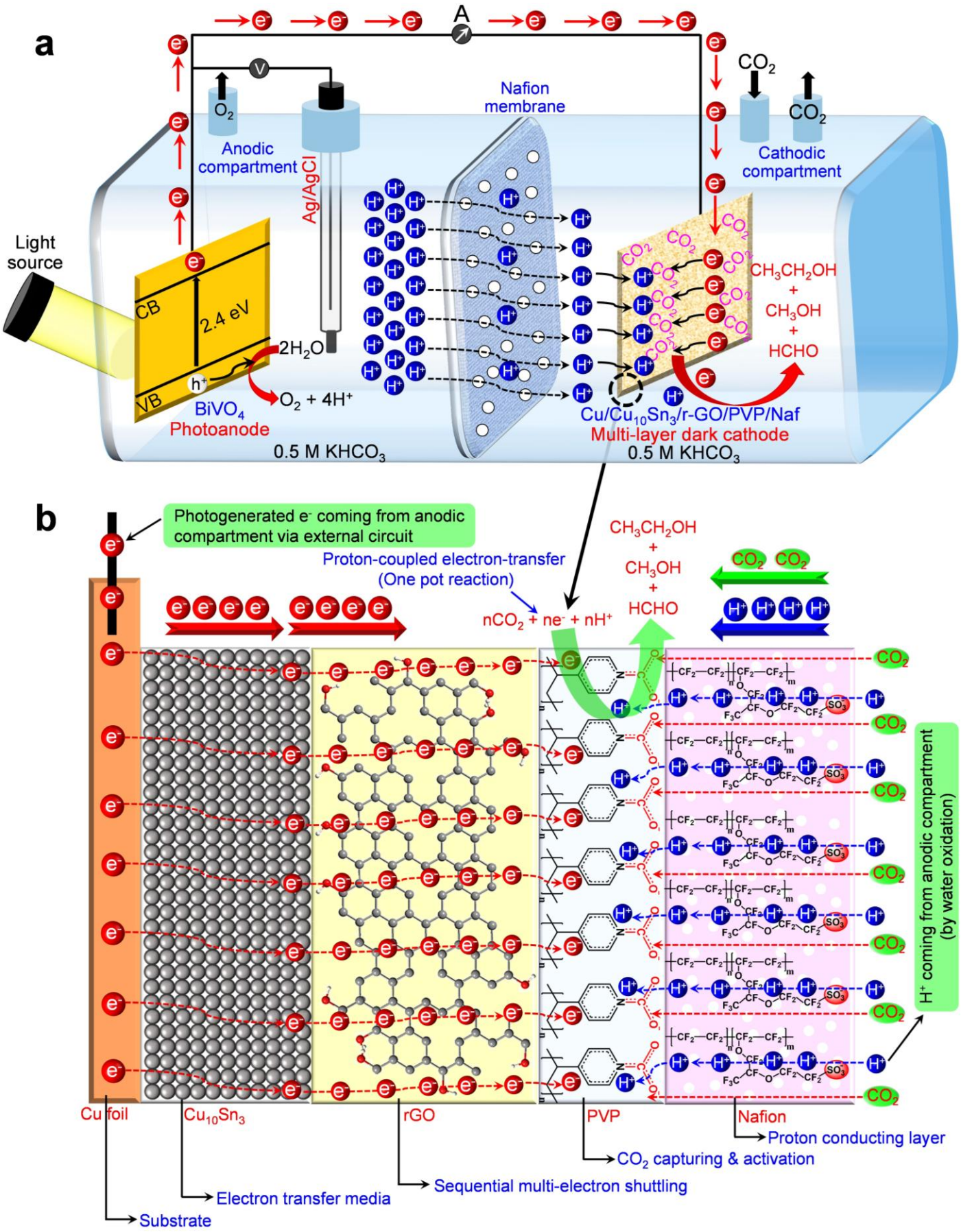
Enhancing proton availability at the CO_2 reduction sites is essential for improving PEC CO_2RR efficiency in solar liquid fuel production. One effective strategy involves coating the cathode with a proton-conductive Nafion layer, which facilitates rapid proton transport to the CO_2 reduction sites.[43-45] Kang et al. demonstrated that Nafion-coated ZnO and TiO_2 thin-film cathodes exhibited high photocurrent densities due to accelerated proton transport through the Nafion layer.[30-32] Nafion is a specialized polymer composed of a fluorocarbon (polytetrafluoroethylene) backbone and sulfonated chains forms interconnected hydrophilic channels that facilitate efficient proton transport to the CO_2 reduction sites. The protons are generated in the anodic compartment through the water oxidation reaction and subsequently diffuse across the chamber-bisecting Nafion membrane into the cathodic compartment, driven by a concentration gradient. However, the proton transfer rate is significantly slower than electron transfer, as electrons move rapidly through an external circuit under applied bias potential, whereas protons must diffuse through the Nafion membrane from the anodic to the cathodic compartment by concentration gradient. The final Nafion coating layer facilitates the rapid protons transport to the CO_2 reduction sites due to its superior proton-conducting properties. Finally, electrons and protons are simultaneously transported to CO_2 reduction sites [$PVP^{\delta+}$-$CO_2^{\delta-}$] in opposite directions *via* different transport pathways, thereby significantly enhances the efficiency of solar liquid fuel production while simultaneously suppressing the HER (Scheme 1).

In this study, we developed a highly efficient PEC CO_2RR system comprising a single-crystalline (040)-faceted $BiVO_4$ photoanode and a Cu/$Cu_{10}Sn_3$/rGO/PVP/Nafion MLDC, which enabled the selective conversion of CO_2 into solar liquid fuels, including methanol, ethanol, and formaldehyde with a remarkably high faradaic efficiency (~91.80%) and solar-to-fuel conversion efficiency (~1.78%) under one-sun illumination (100 mW/cm^2). Furthermore, the formation of key reaction intermediates and products during CO_2RR were systematically monitored by *in-situ* spectroscopic techniques, including *in-situ* Raman, *in-situ* ATR-IR and EPR. To further elucidate the reaction pathways and thermodynamics, density functional theory (DFT) calculations were performed to evaluate Gibbs free energy changes associated with key adsorbed intermediates, providing deeper mechanistic insight into the reaction thermodynamics and underlying mechanisms.

Single-crystalline (040)-faceted $BiVO_4$ photoanode and Cu/$Cu_{10}Sn_3$/rGO/PVP/Nafion multi-layer dark cathode system for selective conversion of CO_2 into solar liquid fuel

Single-crystalline (040)-facet-engineered $BiVO_4$ photoanode facilitated efficient photogeneration and separation of charge carriers under one sun illumination (100 mW/cm^2), wherein the photogenerated electrons were transported through an external circuit and accumulated on the cathode surface, while the photogenerated holes oxidized the water molecules to produce oxygen and protons (Scheme 1). The generated protons subsequently diffuse from the anodic to the cathodic compartment through the Nafion membrane, driven by the established concentration gradient (According to Fick's law of diffusion). However, the proton transport rate remained inherently slower than that of the electrons. To overcome this disparity and ensure efficient proton availability at the electrode/electrolyte interface, an additional Nafion layer was strategically incorporated on the cathode surface to promote rapid proton transport towards the CO_2 reduction site. Each layer of the optimized multi-layer dark cathode enables a distinct and synergistic function during PEC CO_2RR process. The $Cu_{10}Sn_3$ bimetallic alloy facilitates efficient electron transfer from Cu substrate to rGO layer. The rGO serves as a sequential multi-electron shuttling due to its unique high charge-storage capacity and optimal electronic conductivity. The PVP interlayer promotes CO_2 capture and activation by forming a charge-separated [$PVP^{\delta+}$-$CO_2^{\delta-}$] complex, thereby lowering both the reaction overpotential and activation energy of

CO_2RR. Finally, the Nafion overlayer facilitates efficient proton transport to the CO_2 reduction site. This strategic modification enabled synchronized electron-proton coupled transport at the CO_2RR site of PVP layer, where the accumulated charge carriers drive the selective conversion of CO_2 into solar liquid fuels, as illustrated in Scheme 1 and Supplementary Fig. 1.



Scheme 1. Schematic illustration of the PEC CO_2RR system and proposed reaction mechanism. a,

Schematic diagram of the PEC CO_2RR system comprising a single-crystalline (040)-facet-engineered $BiVO_4$ photoanode and a Cu/$Cu_{10}Sn_3$/rGO/PVP/Naf multi-layer dark cathode. **b**, Illustration of the proposed CO_2RR pathway and mechanism on the multi-layer cathode surface, showing sequential multi-electron/multi-proton transfer processes leading to the selective formation of solar liquid fuels, including methanol, ethanol, and formaldehyde.

PEC CO_2RR to solar liquid fuel using a single-crystalline (040)-facet $BiVO_4$ photoanode and various kinds of dark cathodes

PEC CO_2RR was performed in a dual-compartment H-type cell (Artificial Photosynthesis cell; AP cell) separated by a Nafion membrane and equipped with quartz windows (Supplementary Figs. 1,2). A single-crystalline (040)-facet-engineered $BiVO_4$ photoanode was coupled with various dark cathodes and tested under 1 sun illumination (100 mW cm^{-2}) at an applied bias of 1.2 V vs. Ag/AgCl in CO_2-saturated 0.5 M $KHCO_3$ electrolyte for 1 hour (Fig. 1). The base electrode such as Cu/$Cu_{10}Sn_3$ dark cathode produced 8.9 μM ethanol, 18.6 μM methanol, and 211.1 μM formaldehyde. Incorporation of rGO significantly increased yields to 45.9 μM ethanol, 141.6 μM methanol, and 320.8 μM formaldehyde, emphasizing rGO role in the sequential multi-electron transport to the CO_2 reduction sites. Further enhancement was achieved by adding a PVP layer, boosting ethanol and methanol to 78.3 μM and 186.4 μM, respectively, and formaldehyde to 438.5 μM, emphasizing PVP role in the capturing and activating CO_2 reactant molecules *via* charge-separated complex ([$PVP^{\delta+}$-$CO_2^{\delta-}$]). The highest yields were observed with the Cu/$Cu_{10}Sn_3$/rGO/PVP/Nafion MLDC, produced 89.4 μM ethanol, 198.6 μM methanol, and 516.4 μM formaldehyde, emphasizing Nafion role in the efficient transport of protons to the CO_2 reduction sites (Fig. 1a,b and Supplementary Figs. 3,4). GC spectra revealed intense and well-resolved peaks corresponding to each product, with the multilayer configuration showing the highest signal intensity and selectivity (Fig. 1c). Hydrogen gas was also detected as a minor competing product under the same conditions (Fig. 1d-f, Supplementary Figs. 5,6).

To verify that the solar liquid fuel products originated from the reduction of CO_2, isotope-labeling experiments were conducted using $^{12}CO_2$- and $^{13}CO_2$-sat. 0.5 M $KHCO_3$ electrolytes under identical PEC conditions. GC-MS analyses showed clear molecular ion peak shifts: from m/z = 32 (for $^{12}CH_3OH$) to m/z = 33 (for $^{13}CH_3OH$), and from m/z = 46 (for $^{12}C_2H_5OH$) to m/z = 47 (for $^{13}C_2H_5OH$), confirming product

formation from reactant CO_2 gas (Fig. 1g). ^{13}C NMR spectra exhibited signals at 17, 49, and 58 ppm corresponding to $^{13}CH_3CH_2OH$, $^{13}CH_3OH$, and $CH_3{}^{13}CH_2OH$, respectively, which were absent in control experiments with $^{12}CO_2$ (Fig. 1h). ^{1}H NMR (C-H coupling) spectra also exhibits characteristic splitting patterns arising from ^{13}C-^{1}H scalar coupling, clearly visible in the methanol and ethanol resonances, whereas no such coupling is observed for the products derived from $^{12}CO_2$ (Fig. 1i and Supplementary Figs. 7,8). These findings confirm that methanol and ethanol production arises solely from CO_2 reduction, with no contribution from carbonaceous contaminants. The base Cu/$Cu_{10}Sn_3$ cathode showed a Faradaic efficiency (FE) of ~29.9% and a solar-to-fuel (STF) efficiency of ~0.43%. In sharp contrast, the incorporation of rGO, PVP, and Nafion into the multi-layer dark cathode architecture dramatically boosted the FE to ~91.8% and the STF efficiency to ~1.78%, representing one of the highest STF values reported under comparable PEC operating conditions (Fig. 1b,j and Supplementary Tables 1,6,7).[33-44] These results underscore the critical role of interfacial engineering, highlighting the functional significance of each layer. Collectively, this multi-layered architecture synergistically enhances PEC CO_2RR performance, enabling the selective and high-yield production of solar liquid fuels. The functional significance of each layer is discussed in detail in the following subsections.

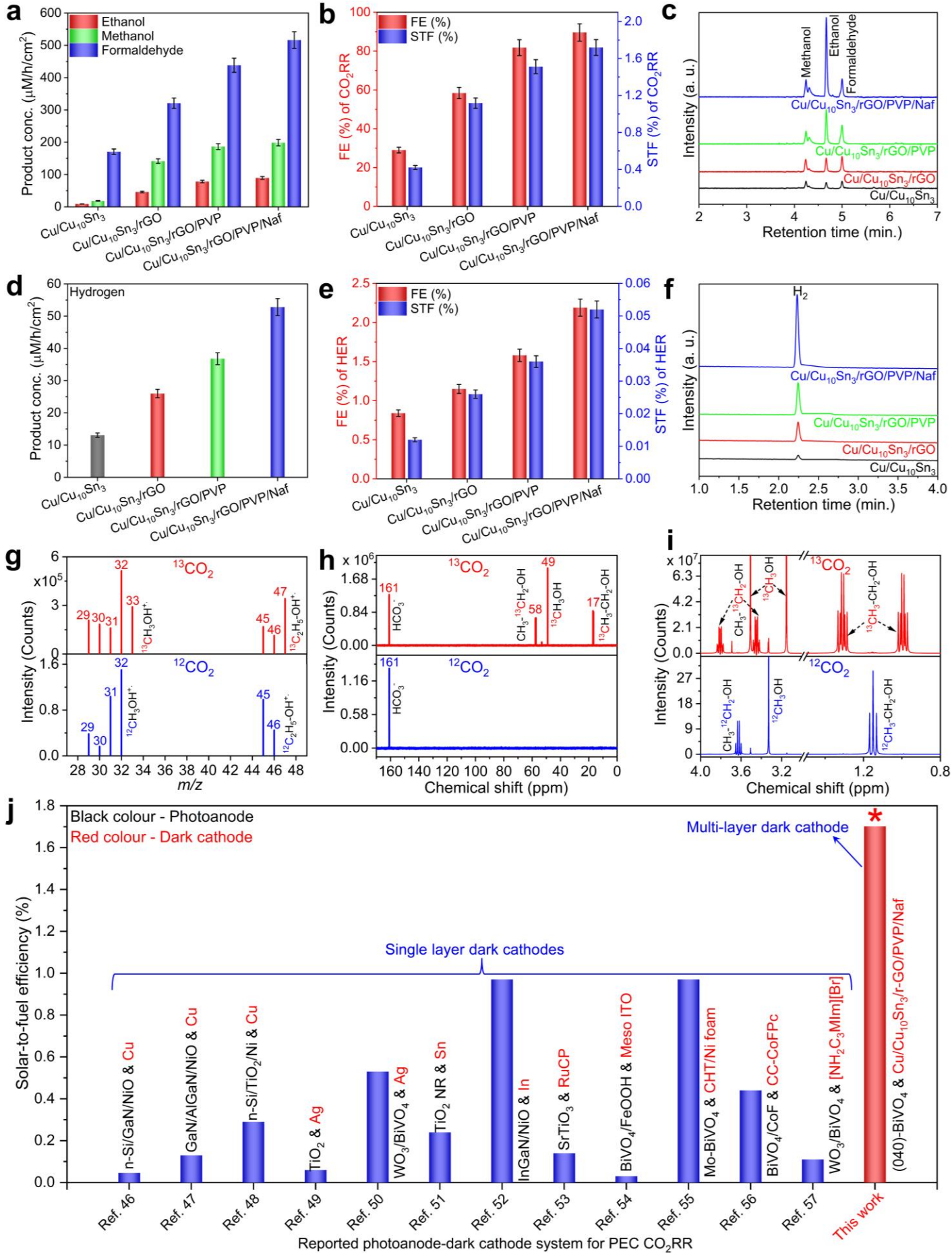

a
Ethanol
Methanol
Formaldehyde
Product conc. (μM/h/cm²)
Cu/Cu10Sn3
Cu/Cu10Sn3/rGO
Cu/Cu10Sn3/rGO/PVP
Cu/Cu10Sn3/rGO/PVP/Naf
b
FE (%)
STF (%)
FE (%) of CO2RR
STF (%) of CO2RR
c
Methanol
Ethanol
Formaldehyde
Intensity (a. u.)
Retention time (min.)
d
Hydrogen
e
FE (%) of HER
STF (%) of HER
f
H2
g
13CO2
12CO2
Intensity (Counts)
m/z
h
Chemical shift (ppm)
i
j
Black colour - Photoanode
Red colour - Dark cathode
Multi-layer dark cathode
Single layer dark cathodes
Solar-to-fuel efficiency (%)
n-Si/GaN/NiO & Cu
GaN/AlGaN/NiO & Cu
n-Si/TiO2/Ni & Cu
TiO2 & Ag
WO3/BiVO4 & Ag
TiO2 NR & Sn
InGaN/NiO & In
SrTiO3 & RuCP
BiVO4/FeOOH & Meso ITO
Mo-BiVO4 & CHT/Ni foam
BiVO4/CoF & CC-CoFPc
WO3/BiVO4 & [NH2C3MIm][Br]
(040)-BiVO4 & Cu/Cu10Sn3/r-GO/PVP/Naf
Ref. 46
Ref. 47
Ref. 48
Ref. 49
Ref. 50
Ref. 51
Ref. 52
Ref. 53
Ref. 54
Ref. 55
Ref. 56
Ref. 57
This work
Reported photoanode-dark cathode system for PEC CO2RR

Figure 1 | Quantitative analysis of PEC CO_2RR and benchmarking solar fuel production. a, Quantitative analysis of solar liquid fuel products including ethanol, methanol, and formaldehyde produced over different dark cathode configurations during 1-hour PEC CO_2RR at 1.2 V vs. Ag/AgCl under 1 sun illumination (100 mW cm^{-2}) in a three-electrode configuration using a (040)-faceted $BiVO_4$ photoanode and various dark cathodes in a CO_2-saturated 0.5 M $KHCO_3$ electrolyte, as determined by gas chromatography with flame ionization detector (FID). **b,** Total Faradaic efficiency (FE) and solar-to-fuel (STF) conversion efficiency of different dark cathode systems for PEC CO_2RR. **c**, Representative GC spectra of CO_2 reduction products collected after 1 hour of PEC CO_2RR. **d,** Hydrogen gas evolution over different dark cathode configurations during 1 h PEC CO_2RR, also analyzed *via* gas chromatography with thermal conductivity detector (TCD). **e**, Comparison of FE and STF efficiency of different dark cathode systems for H_2 evolution reaction. **f**, Representative GC spectra illustrating the evolution of H_2 during 1-hour PEC CO_2RR using different dark cathodes, a TCD detector calibrated with standard H_2 gas mixtures. **g-i,** Isotope labelling experiments were conducted at 1.2 V vs. Ag/AgCl for 12 h using $^{12}CO_2$-saturated 0.5 M $KH^{12}CO_3$ and $^{13}CO_2$-saturated 0.5 M $KH^{13}CO_3$ electrolyte (pH 7.3) to confirm that solar liquid fuels were generated from the reactant CO_2 using (g) GC-MASS, (h) proton-decoupled ^{13}C NMR and (i) ^{1}H NMR (C-H coupling), respectively. **j,** Benchmarking of PEC CO_2RR performance for the (040)-$BiVO_4$ photoanode comprising with Cu/$Cu_{10}Sn_3$/rGO/PVP/Nafion multi-layer dark cathode systems against previously reported conventional photoanode - single layer dark cathode systems.

A single-crystalline (040)-facet engineered $BiVO_4$ photoanode: structural features and photoelectrochemical performance

The $BiVO_4$ photoanode was initially fabricated and evaluated for its PEC performance. In parallel, the $Cu_{10}Sn_3$/rGO/PVP/Nafion MLDC was systematically fabricated and characterized to elucidate its structural configuration and functional contributions to PEC CO_2RR into solar liquid fuels, as detailed in subsequent subsections. A crystal facet engineering strategy was employed to fabricate single-crystalline (040)-facet exposed $BiVO_4$ photoanode to enhance PEC performance by promoting efficient photon absorption and charge carrier separation. The photoanode with a plate-like morphology was vertically grown on the surface of the FTO substrate by a simple seed layer-assisted hydrothermal method using $TiCl_3$ as a structure-directing agent. The FE-SEM image confirms the vertical growth of (040)-faceted $BiVO_4$ plates with an average length of approximately 1.76 μm and diameter of around 0.35 μm (Fig. 2a and Supplementary Figs. 9-11). Elemental mapping and EDS analysis confirms the uniform distribution of Bi, V, and O in the $BiVO_4$ plates (Supplementary Fig. 10). The cross-sectional FE-SEM image further revealed a vertical plate height of ~2.17 μm (Fig. 2a inset, Supplementary Fig. 11). To gain further insight into the microstructure, the photoanode was milled using the focused ion beam technique and then subjected to HR-TEM and SAED analyses, confirming

the vertical growth and plate-like microstructure, while cross-sectional HR-TEM supported the plate morphology (Fig. 2b-i; Supplementary Figs. 12-14). The HR-TEM analysis reveals well-resolved lattice fringes with interplanar spacings of 0.467 nm and 0.254 nm, assigned to the (110) and (002) planes of the (040)-facet monoclinic scheelite $BiVO_4$, confirming high crystallinity and single-crystalline nature (Fig. 2e,f). The corresponding FFT pattern displays sharp diffraction spots indexed to the (002) and (200) planes of (040)-facet, demonstrating long-range structural order (Fig. 2g). The inverse FFT image further highlights the periodic lattice arrangement, while the line-profile analysis quantifies precise d-spacing of 0.251 nm (Figs. 2h,i). X-ray diffraction showed characteristic peaks for monoclinic scheelite $BiVO_4$ (JCPDS 014-0688), with a prominent reflection at $2\theta = 30.4°$ corresponding to the (040)-facet, affirming its successful exposure (Fig. 2f). These microscopic and crystallographic analyses collectively confirmed the formation of vertically grown, single-crystalline (040)-$BiVO_4$ plates on the FTO substrate. PEC measurements demonstrated that the single-crystalline (040)-facet $BiVO_4$ photoanode shows a high photocurrent density of 1.25 mA/cm^2 at 1.23 V vs. RHE under one sun illumination (Fig. 2g). This enhanced performance was attributed to improved charge separation, charge transfer, and charge collection efficiencies, along with suppressed charge recombination facilitated by the highly active (040)-facet.

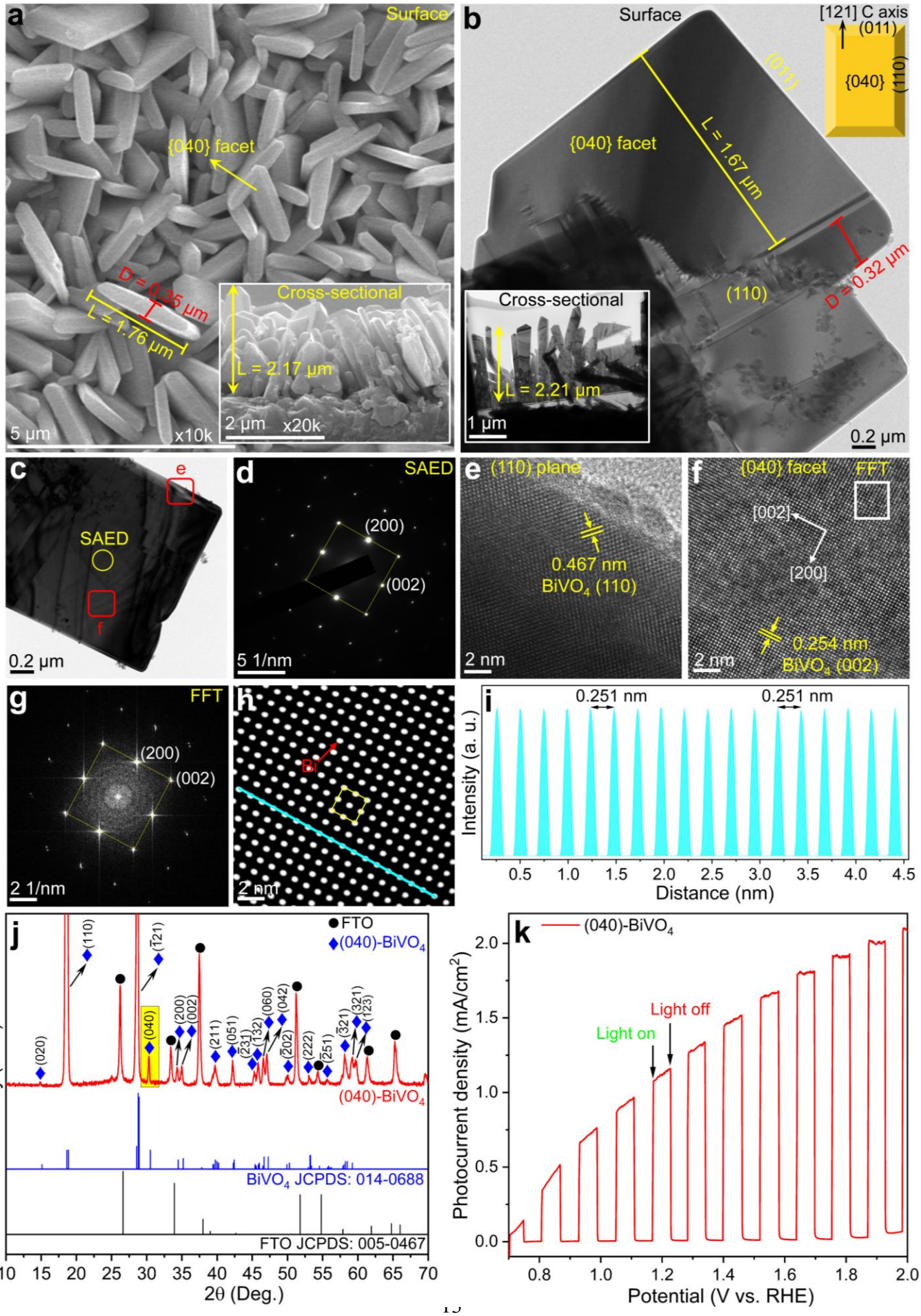

a
Surface
{040} facet
D = 0.35 μm
L = 1.76 μm
Cross-sectional
L = 2.17 μm
2 μm x20k
5 μm x10k
b
Surface
[121] C axis
(011)
{040}
(110)
{040} facet
L = 1.67 μm
D = 0.32 μm
(110)
Cross-sectional
L = 2.21 μm
1 μm
0.2 μm
c
e
SAED
f
0.2 μm
d
SAED
(200)
(002)
5 1/nm
e
(110) plane
0.467 nm
BiVO4 (110)
2 nm
f
{040} facet
FFT
[002]
[200]
0.254 nm
BiVO4 (002)
2 nm
g
FFT
(200)
(002)
2 1/nm
h
Bi
2 nm
i
0.251 nm
0.251 nm
Intensity (a. u.)
Distance (nm)
j
FTO
(040)-BiVO4
(110)
(121)
(020)
(040)
(200)
(002)
(211)
(051)
(231)
(132)
(060)
(042)
(202)
(222)
(251)
(321)
(123)
(040)-BiVO4
BiVO4 JCPDS: 014-0688
FTO JCPDS: 005-0467
Intensity (a. u.)
2θ (Deg.)
k
(040)-BiVO4
Light off
Light on
Photocurrent density (mA/cm2)
Potential (V vs. RHE)

Fig. 2 | Morphological, structural characterization and PEC activity of (040)-$BiVO_4$ photoanode. a, FE-SEM image showing the surface morphology of the (040)-$BiVO_4$ photoanode, with vertically aligned plate-like microstructures; the inset shows a cross-sectional image confirming vertical growth on the FTO substrate. **b**, Low-magnification TEM image displays the plate-like morphology of the (040)-$BiVO_4$ microcrystals, offering further insight into their lateral dimensions and surface uniformity; the inset shows a cross-sectional TEM image obtained after focused ion beam (FIB) milling confirms vertical growth of $BiVO_4$ plates along the (040) crystallographic orientation, indicating preferential facet exposure. **c,d,** Low-magnification of TEM image and their corresponding SAED pattern displays sharp, well-ordered diffraction spots, corroborating the single-crystalline nature of the vertically grown $BiVO_4$ plates. **e,f,** HR-TEM images reveal well-defined lattice fringes with interplanar spacings of 0.467 nm and 0.295 nm, corresponding to the (110) and (002) reflection planes of the (040) facet of monoclinic scheelite $BiVO_4$. **g,** Fast Fourier Transform (FFT) pattern of the selected region HR-TEM region clearly shows distinct diffraction spots and confirming their long-range structural order. **h**, Inverse FFT image of the same region highlights the periodic arrangement of lattice fringes. **i**, Line-profile analysis of the inverse FFT image quantifies the d-spacing. **j**, XRD pattern identifies the monoclinic scheelite phase (space group I2/a) of $BiVO_4$, with a dominant diffraction peak at $2\theta = 30.4°$ corresponding to the (040) plane, indicating successful facet engineering. **k**, Chopped LSV curve showing the PEC performance of the (040)-$BiVO_4$ photoanode under AM 1.5 G one-sun illumination (100 mW cm^{-2}), illustrating efficient light absorption and charge separation.

Time-resolved and mechanistic insights into multi-electron transfer dynamics, CO_2 capture–activation, proton transport, and CO_2RR kinetics

To investigate the functional significance of the multi-layered dark cathode, we first fabricated the Cu/$Cu_{10}Sn_3$/rGO/PVP/Nafion system. This design strategically integrates $Cu_{10}Sn_3$ alloy NPs for efficient electron transfer, rGO for a sequential multi-electron shuttling function, PVP for promoting CO_2 capture and activation, and Nafion overlayer to facilitate efficient proton transport to the CO_2 reduction sites. Initially, $Cu_{10}Sn_3$ alloy NPs were synthesized *via* a co-reduction method and uniformly deposited on Cu foil through drop-casting method (Supplementary Note 1, Figs. 15-17). TEM analysis revealed well-dispersed spherical $Cu_{10}Sn_3$ alloy NPs with an average diameter of ~22.4 nm (Fig. 3a, Supplementary Figs. 18,19), indicating successful colloidal stabilization. The morphological, structural and phase composition of $Cu_{10}Sn_3$ alloy NPs were systematically characterized using various techniques such as XRD, FE-SEM, HR-TEM and XPS, the results are discussed in Supplementary Note 2 and depicted in Supplementary Fig. 19. Following the deposition of the $Cu_{10}Sn_3$ alloy layer as an electron transfer medium, a thin rGO layer was subsequently coated onto the Cu/$Cu_{10}Sn_3$ surface, serving as an efficient electron mediator (Fig. 3a; Supplementary Figs. 15 and 16). The multi-electron accumulation and sequential multi-electron transfer behaviour of rGO were systematically

investigated using time-resolved chronoamperometry (TR-CA), time-resolved photoluminescence (TR-PL) and electrochemical double-layer capacitance (C_{dl}) analysis (Fig. 3c-i, Supplementary Figs. 20,21). To evaluate the multi-electron accumulation and transfer properties of rGO, a thin rGO film was dip-coated onto an Au ultra-microelectrode, and its TR-CA response was recorded in a CO_2-saturated 0.1 M KOH solution. For comparative benchmarking, TR-CA measurements were also conducted using ethylphenothiazine (EPT) and N-ethyl-3,7-dimethoxyphenothiazine (DMeOEPT), well-known one-electron and two-electron redox mediators, respectively, also coated on Au ultra-microelectrodes under identical conditions. Compared to the conventional one-electron (EPT) and two-electron (DMeOEPT) redox mediators, rGO exhibits markedly superior electron transfer performance, ultimately enabling multi-electron transfer which is crucial for the formation of methanol, ethanol and formaldehyde products during PEC CO_2RR (Fig. 3c). The transient current behavior demonstrates the ability of rGO to capture and accumulate electrons *via* a non-Faradaic mechanism and subsequently deliver them through a Faradaic process to the CO_2 reduction sites. The TR-CA results strongly indicate that the rGO layer deposited on the surface of Cu/$Cu_{10}Sn_3$ electrode modulates electron-transfer kinetics through its high charge-storage capacity and excellent electronic conductivity, thereby extending the lifetime of reaction intermediates and facilitating subsequent electron-transfer steps.

To gain further mechanistic insights of rGO, TR-PL decay and 2D fluorescence mapping were conducted (Fig. 3d-f). The $Cu_{10}Sn_3$ alloy exhibited a photogenerated electron lifetime of 3.30 ns, which significantly decreased to 2.21 ns upon rGO deposition (Fig. 3d). The π-conjugated network of rGO enables high conductivity and storage capacity, facilitating delocalization of accumulated electrons and sequential multi-electron transfer to the CO_2 reduction sites. This behaviour is clearly visualized in the 2D TR-PL fluorescence maps. The Cu/$Cu_{10}Sn_3$ shows minimal electron retention, reflected by a low-intensity signal (dark), whereas the $Cu_{10}Sn_3$/rGO exhibits a significantly higher electron density, with a blue/green emission pattern indicative of enhanced charge accumulation (Fig. 3e,f). To further confirm the charge accumulation behaviour of the rGO interlayer, electrochemical double-layer capacitance (C_{dl}) was estimated using cyclic voltammetry at different scan rates in the non-Faradaic region (Supplementary Figs. 20,21). The base

$Cu/Cu_{10}Sn_3$ electrode exhibited a relatively low C_{dl} of 12.3 μF cm^{-2} (electrochemical active surface area; ECSA = 0.31 cm^2), indicating limited interfacial charge storage capacity, whereas the C_{dl} value increased dramatically to 107.9 μF cm^{-2} (ECSA = 2.69 cm^2) upon deposition of the rGO layer, confirming substantial enhancement in interfacial capacitance. This enhancement originated from extended π-electron system of rGO and high electrochemically active surface area, enabling it to function as a dynamic electron reservoir. The TR-CA and TR-PL results clearly demonstrate that rGO facilitates efficient sequential multi-electron transfer and charge accumulation, key to boosting CO_2RR efficiency and product selectivity. The structural and functional contributions of subsequent PVP and Nafion layers are discussed in the following sections.

The electrochemical activity of as-fabricated dark cathodes was systematically evaluated using linear sweep voltammetry (LSV), cyclic voltammetry (CV), and electrochemical impedance spectroscopy (EIS), the corresponding results are discussed in Supplementary Note 3 and presented in Supplementary Fig. 22. To optimize the PVP interlayer for efficient CO_2 capturing and activation, EIS Nyquist plots were obtained at -0.5 V vs. Ag/AgCl for $Cu/Cu_{10}Sn_3$/rGO cathodes coated with PVP of varying thickness (Fig. 3g,i and Supplementary Fig. 23). The results indicate that electron transfer from rGO to the CO_2 reduction sites of PVP layer ([$PVP^{\delta+}$-$CO_2^{\delta-}$] complex) occurs with a slightly increased energy barrier due to the intrinsic insulating nature of PVP layer. Among the tested loadings, the 3 wt% PVP layer (~1026 nm thick) exhibited the lowest charge-transfer resistance, as evidenced by the smallest Nyquist semicircle diameter, and consequently the lowest activation energy. In contrast, thinner (0.1 wt%) and thicker (5 wt%) PVP layers exhibited higher impedance due to insufficient [$PVP^{\delta+}$-$CO_2^{\delta-}$] complex formation and restricted electrolyte penetration, respectively. This confirms that the 3 wt% PVP is the optimum composition for facilitating rapid electron transfer through the PVP matrix by effectively balancing its electronic insulation with the chemical activation of CO_2. (Fig. 3i). In the next step, to enhance the proton availability at the CO_2 reduction sites, a Nafion overlayer was deposited on top of the PVP layer. Porous Nafion served as a proton-conductive polymeric layer that enabled the efficient transfer of H^+ to the CO_2 reduction sites. EIS analysis of $Cu/Cu_{10}Sn_3$/rGO/PVP cathodes with varying Nafion thickness revealed that a 15 wt% Nafion film (~4736 nm, confirmed by cross-

sectional FE-SEM; Fig. 3h,j and Supplementary Fig. 24) shows the lowest proton-transfer resistance. Conversely, the thinnest Nafion layer (1.0 wt%, ~1157 nm) displayed poor conductivity due to coating defects, resulting in the largest impedance response. Thus, thick and defect-free Nafion coating (15 wt%, 4736 nm) enabled efficient proton delivery to the CO_2 reduction sites as well as enhanced the stability of multi-layer cathode.

The PVP interlayer significantly lowers both the reaction overpotential and activation energy for CO_2RR by facilitating the capture and activation of CO_2 molecules in their reactant state. The mechanistic role of the PVP interlayer in lowering the CO_2RR reaction overpotential was investigated through Tafel slope analysis. The optimized 3 wt% PVP layer facilitated CO_2 activation by forming a charge-separated [$PVP^{\delta+}$-$CO_2^{\delta-}$] complex, thereby lowering the energy barrier for the first electron-transfer step. This activation step effectively elevated the CO_2 molecules to a higher-energy reactive state, thereby lowering the activation barrier for the rate-determining first electron-transfer step. Tafel analysis revealed that the Cu/$Cu_{10}Sn_3$/rGO/PVP/Naf MLDC exhibited a markedly lower reaction overpotential (11.06 kJ mol^{-1}) compared to the base Cu/$Cu_{10}Sn_3$ cathode (19.64 kJ mol^{-1}), confirming the crucial role of PVP layer in facilitating CO_2 activation and reducing the kinetic energy barrier (Supplementary Fig. 25). Moreover, the activation energy for the rate determining first-electron transfer step was investigated using Arrhenius equation (Eqn.1-3) through temperature-dependent EIS analysis (Supplementary Fig. 26).

$$K = A\, e^{-Ea/RT} \dots\dots\dots\dots\dots\dots\dots\dots\dots\dots (1)$$

$$Ln(K) = Ln\,(A) - \frac{Ea}{RT} \dots\dots\dots\dots\dots\dots\dots\dots (2)$$

$$Ln\,\left(\frac{1}{R}\right) = -\frac{Ea}{R}\left(\frac{1000}{T}\right) + Ln\,(A) \dots\dots\dots (3)$$

The optimized Cu/$Cu_{10}Sn_3$/rGO/PVP/Naf MLDC exhibited a significantly lower activation energy (34.75 kJ mol^{-1}) compared to base Cu/$Cu_{10}Sn_3$ cathode (48.55 kJ mol^{-1}), as shown in Supplementary Fig. 26. The activation energy data derived from the Arrhenius equation strongly suggest that PVP interlayer decreases the activation energy of rate-determining first-electron transfer step in CO_2RR. The optimized 3 wt% PVP layer provides abundant adsorption sites for CO_2 molecules and simultaneously activates them in the reactant

state through complexation with nitrogen atoms of the pyridine rings in the PVP matrix. This complexation induces intramolecular charge separation, resulting in the formation of a [$PVP^{\delta+}$-$CO_2^{\delta-}$] complex in the reactant state. This interaction effectively activates the CO_2 molecule by elevating it to a higher thermodynamic energy level and substantially lowers the activation energy of the rate-determining first electron transfer step in CO_2RR (Fig. 3k,l). In conclusion, the combination of rGO and Nafion layers enhanced the rates of sequential multi-electron and multi-proton transfer to the CO_2 reduction sites, respectively, thereby promoting ethanol formation through the dimerization of carbon-centered intermediates (*C≡O), as illustrated in Scheme 2. The sequential multi-electron/multi-proton transfer led to a change in product selectivity from methanol (*via* $6e^-/6H^+$ transport) to ethanol (*via* $12e^-/12H^+$ transport). The change in product from methanol to ethanol was enabled by the extended adsorption lifetime of reaction intermediates, which facilitated both the dimerization of carbon-centered radicals and sustained multi-electron/multi-proton transfer processes (Fig. 3k,l). Collectively, these findings underscore the synergistic roles of the rGO, PVP and Nafion layers in modulating charge transfer dynamics and selectivity in PEC CO_2RR system.

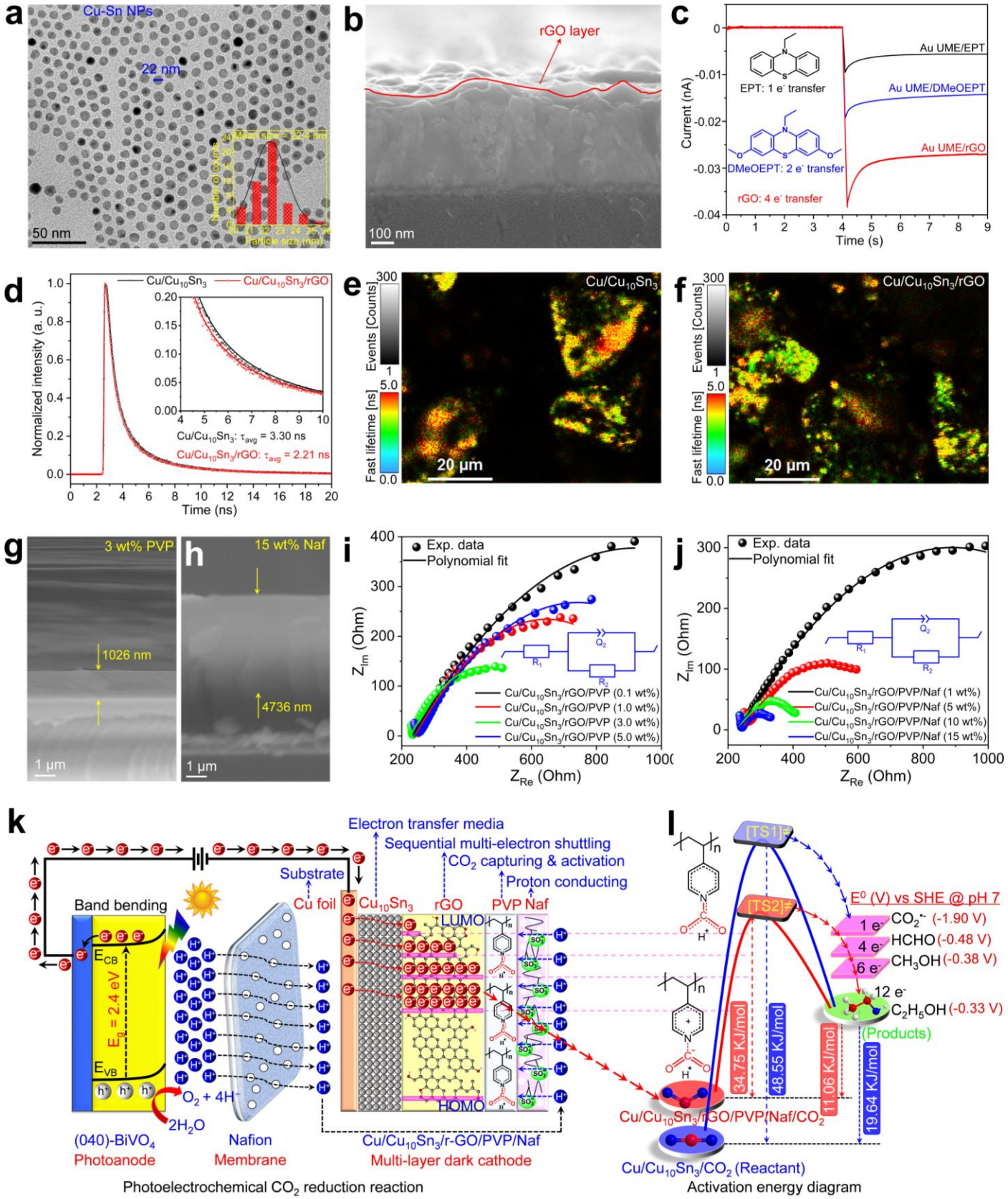


Fig. 3 | HR-TEM and cross-sectional FE-SEM characterization, time-resolved PL/CA analysis of multi-electron transfer, and kinetic evaluation of CO_2RR overpotential and activation energy of $Cu/Cu_{10}Sn_3$-based dark cathodes. a, Low-magnification TEM image of monodisperse $Cu_{10}Sn_3$ alloy NPs reveal uniform spherical morphology with an average particle diameter of ~22.4 nm. **b**, Cross-sectional FE-SEM image

showing the morphology of the rGO layer uniformly deposited over the $Cu_{10}Sn_3$ alloy surface, forming a continuous and conductive interface. **c**, Time-resolved chronoamperometric (TR-CA) measurements conducted on rGO-coated Au ultramicroelectrodes in CO_2-saturated 0.1 M KOH electrolyte with redox mediators ethylphenothiazine (EPT) and N-ethyl-3,7-dimethoxyphenothiazine (DMeOEPT) demonstrate rapid multi-electron shuttling behavior of the rGO layer. **d,** Time-resolved photoluminescence (TR-PL) decay curves of $Cu/Cu_{10}Sn_3$ and $Cu/Cu_{10}Sn_3$/rGO electrodes, excited at 375 nm using a picosecond pulsed diode laser. **e,f,** Two-dimensional TR-PL fluorescence maps of $Cu/Cu_{10}Sn_3$ (e) and $Cu/Cu_{10}Sn_3$/rGO (f) electrodes. **g**, Cross-sectional FE-SEM image showing the morphology and thickness of PVP layer coated on FTO substrate with 3 wt% PVP. **h**, Cross-sectional FE-SEM image illustrating the thickness of Nafion film deposited on FTO substrate with 15 wt% Naf. **i**, Nyquist plots of $Cu/Cu_{10}Sn_3$/rGO dark cathodes coated with different wt% of PVP layers (0.1-5 wt%) recorded at a fixed potential of -0.58 V vs. RHE using CO_2-saturated 0.5 M $KHCO_3$ electrolyte. **j**, Nyquist plots were acquired for $Cu/Cu_{10}Sn_3$/rGO/PVP multi-layer dark cathodes coated with Nafion films of varying concentrations (1, 5, 10, and 15 wt%) in a CO_2-saturated 0.5 M $KHCO_3$ electrolyte at a fixed applied potential of -0.58 V vs. RHE. **k**, Schematic energy level diagram of CO_2RR pathway for $Cu/Cu_{10}Sn_3$/rGO/PVP/Naf MLDC. **l**, Activation energy diagram of CO_2RR for both $Cu/Cu_{10}Sn_3$ dark cathode (Blue color) cathode and $Cu/Cu_{10}Sn_3$/rGO/PVP/Naf MLDC (Red color).

DFT calculations of Gibbs free energy changes for key reaction intermediates and *in-situ* Raman spectroscopic analysis of local pH variations during CO_2RR

To further elucidate the mechanistic role of PVP interlayer, DFT calculations were performed by evaluating the Gibbs free energy changes associated with key reaction intermediates, supported by *in-situ* Raman, *in-situ* ATR-IR and EPR spectroscopic evidence. The reaction mechanism follows a stepwise proton-coupled electron transfer process, where the nitrogen site in PVP stabilizes reaction intermediates, lowers the activation energy barriers, and enhances CO_2RR activity (Fig. 4a-d). The N-site of PVP plays a key role in stabilizing the reaction intermediates through σ-donation and π-back bonding effects. Initially, CO_2 molecules are captured and activated by N-site of PVP, adsorbing as $*CO_2$ with ΔG = -1.978 eV, stabilized by weak interactions with C-N bond formation. To gain more theoretical insights into the activation of CO_2 molecules and the mechanistic role of PVP in lowering the activation energy barrier of the rate-determining first-electron transfer step of CO_2RR, DFT calculations were performed and the results were discussed in Supplementary note 4 and presented in Supplementary Figs. 27,28. The first protonation step forms *COOH with ΔG = -0.259 eV, followed by subsequent reduction to *C≡O with ΔG = 0.681 eV. For methanol formation, *C≡O undergoes protonation to form *CHO with ΔG = -1.048 eV, the most stabilized intermediate in the methanol production pathway. Further protonation leads to the formation of $*OCH_3$ with ΔG = 3.507 eV, which desorbs as $*OHCH_3$

with ΔG = 0.652 eV, yielding methanol (Figs. 4a,c and Supplementary Table 4). The progressive energy changes indicate that methanol formation follows a relatively endergonic final step, requiring an efficient catalyst surface to facilitate desorption. In contrast, ethanol formation proceeds *via* an alternative mechanistic route. The early-stage intermediates (*CO_2, *COOH, *C≡O) remain similar to the methanol pathway, with *C≡O having ΔG = 0.681 eV. However, a key branching point occurs at the C-C coupling step, where *COCO forms with ΔG = -1.571 eV *via* an exergonic reaction, providing a strong thermodynamic driving force for ethanol selectivity. This step is particularly crucial, as efficient C-C bond formation is a key challenge in CO_2RR. The subsequent protonation steps proceed through *COCOH with ΔG = 0.246 eV, *CHCO + H_2O with ΔG = 2.428 eV, *$OCHCH_2$ with ΔG = -0.873 eV, *OCH_2CH_3 with ΔG = -0.201 eV, ultimately yielding ethanol (*$OHCH_2CH_3$) with ΔG = 1.097 eV (Figs. 4b,d and Supplementary Table 5). These findings highlight the thermodynamic feasibility and mechanistic pathway of methanol and ethanol production and emphasize the importance of N-site of PVP in stabilizing intermediates and promoting C-C coupling for ethanol formation.

The local pH changes at the electrode/electrolyte interface play a critical role in the formation and stabilization of key reaction intermediates, thereby significantly influencing the generation of final products during CO_2RR. The local pH variations strongly affect the key reaction parameters, including product efficiency, selectivity, and intermediate formation and stability. To probe this, *in-situ* Raman spectroscopy was employed to quantitatively monitor the local pH changes at the electrode-electrolyte interface (Supplementary Note 5, Supplementary Figs. 29,30, Supplementary Tables 2,3). To determine the local pH changes, we focused on the two most responsive and well-resolved Raman bands: the $_{\upsilon}$C-OH stretch at 1020 cm^{-1} and the $_{\upsilon}$C-O stretch at 1065 cm^{-1}, corresponding to HCO_3^- and CO_3^{2-}, respectively (Figs. 4e,g and Supplementary Figs. 31,32). The relative intensities of these peaks were used to estimate the $[HCO_3^-]/[CO_3^{2-}]$ concentration ratio at the electrode/electrolyte interface, a key determinant of local pH. A calibration curve was constructed by plotting this intensity ratio as a function of applied potential (Figs. 4f,h and Supplementary Figs. 31,32). Using Henderson-Hasselbalch equation (pKa ≈ 10.33 at 25 °C, Eqn. 4), the local pH changes during CO_2RR and HER was estimated based on the deconvoluted peak areas HCO_3^- and CO_3^{2-}. The local pH gradually increased to

~9.8 during CO_2RR and this alkaline shift arises from proton consumption and OH^- generation, which alters the HCO_3^-/CO_3^{2-} equilibrium. Importantly, the raised interfacial pH suppresses hydrogen evolution and favors the stabilization of CO_2RR intermediates (*COOH, *CO, *CHO, *OCH_2, *OCH_3, *COCO and *OCHO), thus enhancing selectivity toward C_1-C_2 solar fuels (methanol, ethanol, and formaldehyde), as shown in Figs. 4f,h.

$$\mathrm{pH} = \mathrm{pKa} + \log\frac{[{CO_3}^{2-}]}{[{HCO_3}^{-}]} \ldots\ldots\ldots\ldots\ldots\ldots\ldots\ldots\ldots\ldots (4)$$

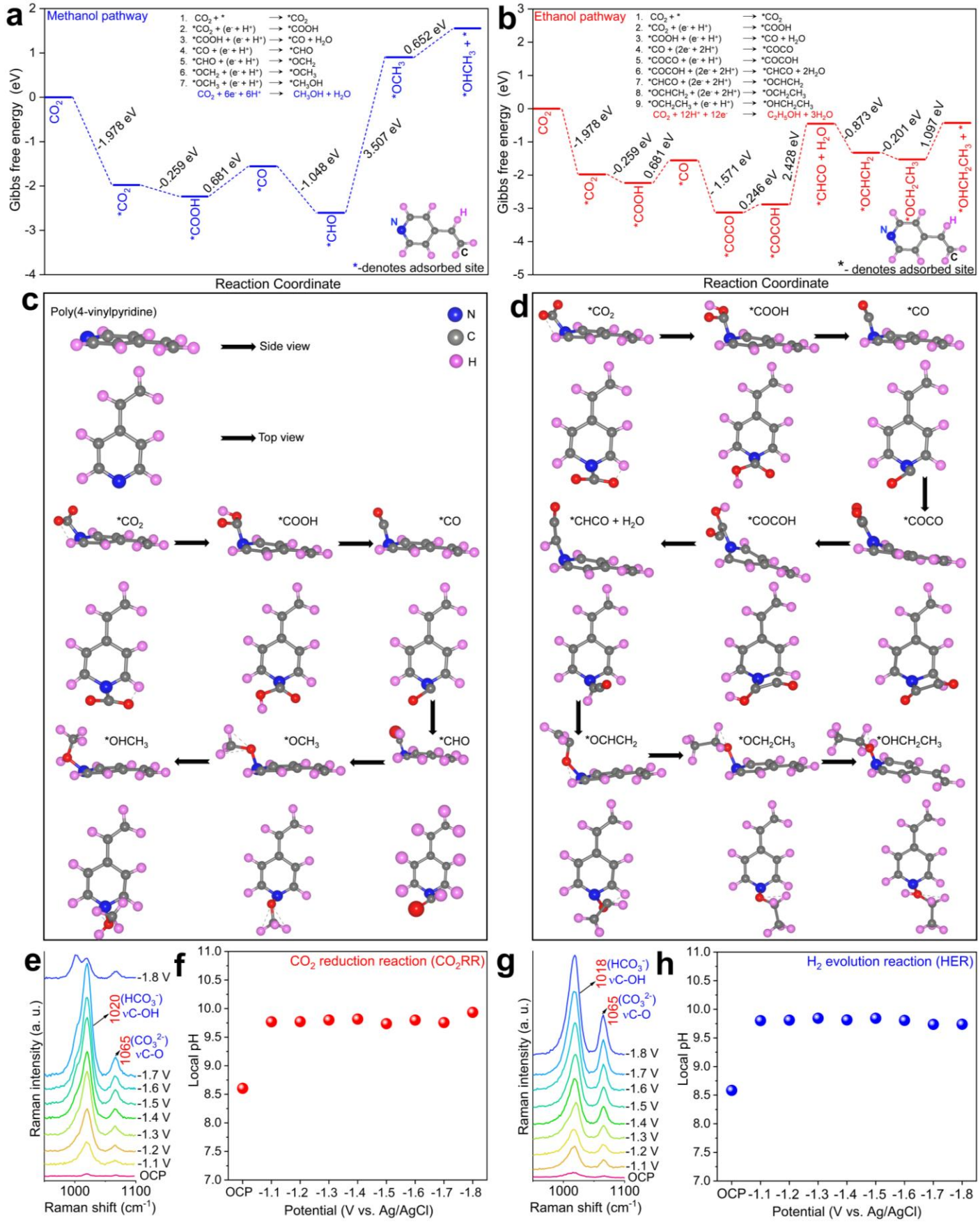


Fig. 4 | DFT calculation of Gibbs free energy changes for key adsorbed intermediates for methanol and ethanol formation pathway and Local pH measurements during CO_2RR using *in-situ* Raman

spectroscopy. a, Gibbs free energy change profile for the CO_2RR pathway toward methanol formation, showing a sequence of proton-coupled electron transfer steps starting from adsorbed *CO_2 to *COOH, *CO, *CHO, and ultimately *OCH_3 and methanol. **b**, Gibbs free energy change profile for ethanol formation *via* a C-C coupling mechanism, includes early-stage intermediates (*CO_2, *COOH, and *CO), followed by dimerization of two *CO species to form *COCO and subsequent reductions yield *COCOH, *CHCO, *$OCHCH_2$ and *OCH_2CH_3 intermediates, leading to ethanol. **c**, Optimized DFT model showing key methanol intermediates adsorbed on the nitrogen site of the PVP surface. **d**, Structural representation of adsorbed intermediates on the nitrogen site of the PVP surface for ethanol formation pathway. **e**, Enlarged Raman spectra collected during CO_2RR in the frequency range of 950-1100 cm^{-1} reveal two diagnostic vibrational modes: the υ(C-OH) stretching of bicarbonate (HCO_3^-) at ~1020 cm^{-1} and the υ(C-O) stretching of carbonate (CO_3^{2-}) at ~1065 cm^{-1}. **f**, The calculated local pH values, plotted as a function of applied potential, reveal a steady increase from near-neutral to moderately alkaline conditions, reaching approximately pH 9.8 under continuous CO_2RR operation in CO_2-saturated 0.5 M $KHCO_3$ electrolyte. **g**, Enlarged *in-situ* Raman spectra acquired during HER in the 950-1100 cm^{-1} region. **h**, The resulting potential-dependent interfacial pH profile demonstrates a pronounced alkaline of the electrode/electrolyte interface under HER conditions in Ar-saturated 0.5 M $KHCO_3$ electrolyte.

Monitoring the formation $CO_2^{\bullet-}$ anion radical, key reaction intermediates and products during CO_2RR using *in-situ* spectroscopic techniques

The reaction pathway and underlying mechanism of CO_2RR, including the identification of key reaction intermediates and final products at the electrode/electrolyte interface, were systematically monitored through *in-situ* Raman, *in-situ* ATR-IR, EPR spectroscopic techniques. Fig. 5a shows the schematic experimental set-up of *in-situ* Raman spectroscopy consisted of 785 nm laser source with 200 mW output power, enabling high-sensitivity detection of vibrational features of the formation of key reaction intermediates and products during CO_2RR. Time- and potential-dependent *in-situ* Raman spectra collected over the Cu/$Cu_{10}Sn_3$/rGO/PVP/Naf MLDC in CO_2-saturated 0.5 M $KHCO_3$ electrolyte revealed progressive changes in vibrational frequencies (Fig. 5a,b and Supplementary Figs. 33-41). Prior to the initiation of the CO_2RR (at 0 min.), several characteristic Raman peaks were observed which are related to the Cu substrate (226 cm^{-1}, $_{\upsilon}$Cu-O stretching), PVP (635, 1190 cm^{-1}), and electrolyte species such as HCO_3^- and CO_3^{2-} (1020, 1065, 1390, 1603 cm^{-1} assigned to $_{\upsilon}$C-OH (HCO_3^-), $_{\upsilon}$C-O (CO_3^{2-}), $_{\upsilon s}$C-O (HCO_3^-) and $_{\upsilon as}$C-O (HCO_3^-)).[45] Upon applying a constant potential of -0.58 V vs. RHE to initiate CO_2RR, several new Raman peaks emerged, indicating the formation of transient key reaction intermediates and products on the surface of the electrode. Notably, a key reaction intermediate monitored at 408 cm^{-1} was attributed to the carboxyl group ($_{\upsilon}$*COOH), which corresponds to the formation of

methanol and ethanol products.[46] In addition, another important intermediate was monitored at 556 cm^{-1} corresponds to the bidentate O-bound υ*OCO* species, which serves as the critical intermediate in the rate-limiting step for formaldehyde generation. Additionally, the Raman peaks appeared at 788, 1288 and 1560 cm^{-1} which were assigned to the bending or deformation mode of $_{\delta}CO_2^-$, $_{\upsilon s}CO_2^-$ and $_{\upsilon as}CO_2^-$ intermediate which strongly suggest that the formation of $CO_2^{\bullet-}$ anion radical during CO_2RR. A $_{\gamma}$C-H bending or deformation mode was observed at 1131 cm^{-1}, further supporting the presence of hydrocarbon intermediates.[47] Importantly, a double-band shape Raman signals were observed at 1454, and 1497 cm^{-1} corresponds to an O-bound bidentate intermediate which originated from the υ*OCH*O species which is responsible for HCHO formation.[48] The most important intermediate species such as υ*C≡O was observed at 2065 cm^{-1}, provides compelling evidence of an intermediate involved in both methanol and ethanol formation.[49] In the case of ethanol formation, this adsorbed υ*C≡O intermediate undergoes dimerization process, ultimately leading to ethanol formation over the MLDC surface (Scheme 2).

To gain deeper mechanistic insight into the CO_2RR, *in-situ* ATR-IR spectroscopy was employed to monitor the vibrational features of key reaction intermediates and products at the electrode/electrolyte interface (Fig. 5c,d and Supplementary Figs. 42-48). Fig. 5c shows the schematic experimental set-up of the *in-situ* ATR-IR which consisted of a germanium (Ge) ATR crystal configured for multiple internal reflections, enabling enhanced signal sensitivity to detect the formation of transient adsorbed intermediates at the electrode/electrolyte interface during CO_2RR. Time- and potential-dependent *in-situ* ATR-IR spectra were recorded over the $Cu_{10}Sn_3$/rGO/PVP/Naf MLDC in the presence of CO_2-saturated 0.5 M $KHCO_3$ electrolyte (Fig. 5d and Supplementary Figs. 44,45). Prior to the initiation of the CO_2RR, no stretching vibration was observed except asymmetric stretching vibrations of $_{\upsilon as}CO_2$ (2360 and 2337 cm^{-1}) at 0 minutes. Upon applying a constant cathodic potential of -0.58 V vs. RHE to initiate CO_2RR, several new IR-active vibrational features emerged progressively with time, signifying the formation and accumulation of key reaction intermediates and products at the electrode/electrolyte interface. A prominent peak was observed at 1643 cm^{-1} corresponds to the asymmetric stretching vibration of the CO_2^- anion intermediate which indicates the initial electron transfer

step. Another dominant peak was observed at 1394 cm^{-1} corresponds to the carboxyl group ($_{\upsilon}$*COOH), a key intermediate species involved in the rate-limiting step toward methanol and ethanol formation.[50] The most important intermediate peak was observed at 1946 cm^{-1} assigned to the $_{\upsilon}$*C≡O, which is the essential intermediate species in the formation of methanol and ethanol products.[51,52] In the case of methanol formation, the adsorbed $_{\upsilon}$*C≡O intermediate sequentially reduced to $_{\upsilon}$*CHO and $_{\upsilon}$*OCH_3 (C-O) which were observed at 1033 and 1150 cm^{-1}, respectively. In the case of ethanol formation, the adsorbed $_{\upsilon}$*C≡O intermediate undergoes dimerization, leading to the formation of a *COCO species, which was observed at 1698 cm^{-1}. This intermediate is subsequently reduced by proton-electron coupling to yield *COCOH, which was observed at 1558 cm^{-1}.[66,53] Most importantly, the direct evidence of C-H stretching and bending vibrations were observed, which strongly confirms the formation of solar liquid fuels during CO_2RR. The IR bands at 2955, 2924, and 2869 cm^{-1} were assigned to the C-H stretching vibrations of methanol, ethanol and formaldehyde, respectively, while a characteristic bending mode at 880 cm^{-1} further confirmed the presence of C-H bonds in the final products.[60,47] Moreover, two additional high-frequency bands at 3382 and 3746 cm^{-1} were observed and assigned to surface hydroxyl (-OH) stretching vibrations or final alcohol products (Scheme 2). This direct spectroscopic evidence strongly suggests that the formation of solar liquid fuels including, methanol, ethanol, and formaldehyde over the surface of Cu/$Cu_{10}Sn_3$/rGO/PVP/Naf MLDC during CO_2RR.

The formation of $CO_2^{\bullet-}$ anion radical intermediates during CO_2RR were confirmed using low-temperature EPR spectroscopy (Fig. 5e,f and Supplementary Figs. 49-52).[26,54] Due to their extremely short lifetime, $CO_2^{\bullet-}$ anion radicals were captured using dimethyl-1-pyrroline N-oxide (DMPO) as a spin-trapping agent, forming stable DMPO-CO_2 adducts (Fig. 5e). Prior to the initiation of the CO_2RR, no EPR signal was observed, however, after 1 hour reaction, EPR spectra shows the multiple signals corresponding to the oxidized DMPO, DMPO-OH adduct, DMPO-OOH adduct, and the DMPO-CO_2 adduct (Fig. 5f).[55] The presence of $CO_2^{\bullet-}$ anion radical intermediates was confirmed by the observation of six hyperfine splitting signals in the EPR spectra, characterized by coupling constants of 15.4 G and 19.2 G for αN and αH nuclei, respectively (Fig. 5f, Supplementary Figs. 51,52).[55] This phenomenon strongly suggests that the formation of $CO_2^{\bullet-}$ anion

radical intermediates during CO_2RR process. Additionally, the EPR spectrum revealed the presence of the DMPO-OH adduct, which displayed four hyperfine splitting signals with a coupling constant of 13.5 G for both αN and αH nuclei (Fig. 5f). Theoretically, the DMPO-OH adduct is expected to exhibit a triplet EPR signal due to the singular nuclear spin (I = 1) of nitrogen. However, the hyperfine splitting associated with nitrogen is further divided into a doublet due to interactions with a neighboring hydrogen nucleus (I = ½). Since the nitrogen and hydrogen atoms within the DMPO-OH adduct exhibit identical coupling constants (αN = αH = 13.5 G), their overlapping signals result in the emergence of four distinct EPR peaks with an intensity ratio of 1:2:2:1 (Fig. 5f, Supplementary Fig. 51,52).[56,57] A similar splitting pattern was observed in the EPR spectrum of the DMPO-OOH adduct, which also displayed four hyperfine splitting signals with a coupling constant of 15.3 G for both αN and αH nuclei. The overlapping signals from nitrogen and hydrogen (αN = αH = 15.3 G) produced four hyperfine splitting signals with an intensity ratio of 1:2:2:1 (Fig. 5f, Supplementary Fig. 51,52).[56,57] In contrast, the DMPO-CO_2 adduct exhibited six hyperfine splitting signals due to a change in the coupling constants of nitrogen and hydrogen nuclei (αN = 15.4 G and αH = 19.2 G) (Fig. 5f, Supplementary Fig. 51,52).[58] Ultimately, the EPR findings provide compelling evidence that the $CO_2^{\bullet-}$ anion radicals were generated through the first-electron transfer from the rGO to [$PVP^{\delta+}$-$CO_2^{\delta-}$] complex. This electron transfer result significantly enhances the reaction kinetics, improves the product selectivity, and effectively leads the CO_2RR process toward the efficient conversion of CO_2 into solar liquid fuels. Finally, the plausible reaction pathway and underlying mechanism for the formation of methanol, ethanol and formaldehyde have been proposed based on experimental evidence obtained from *in-situ* Raman*, in-situ* ATR-IR and EPR spectroscopic techniques as illustrated in Scheme 2 (See next section).

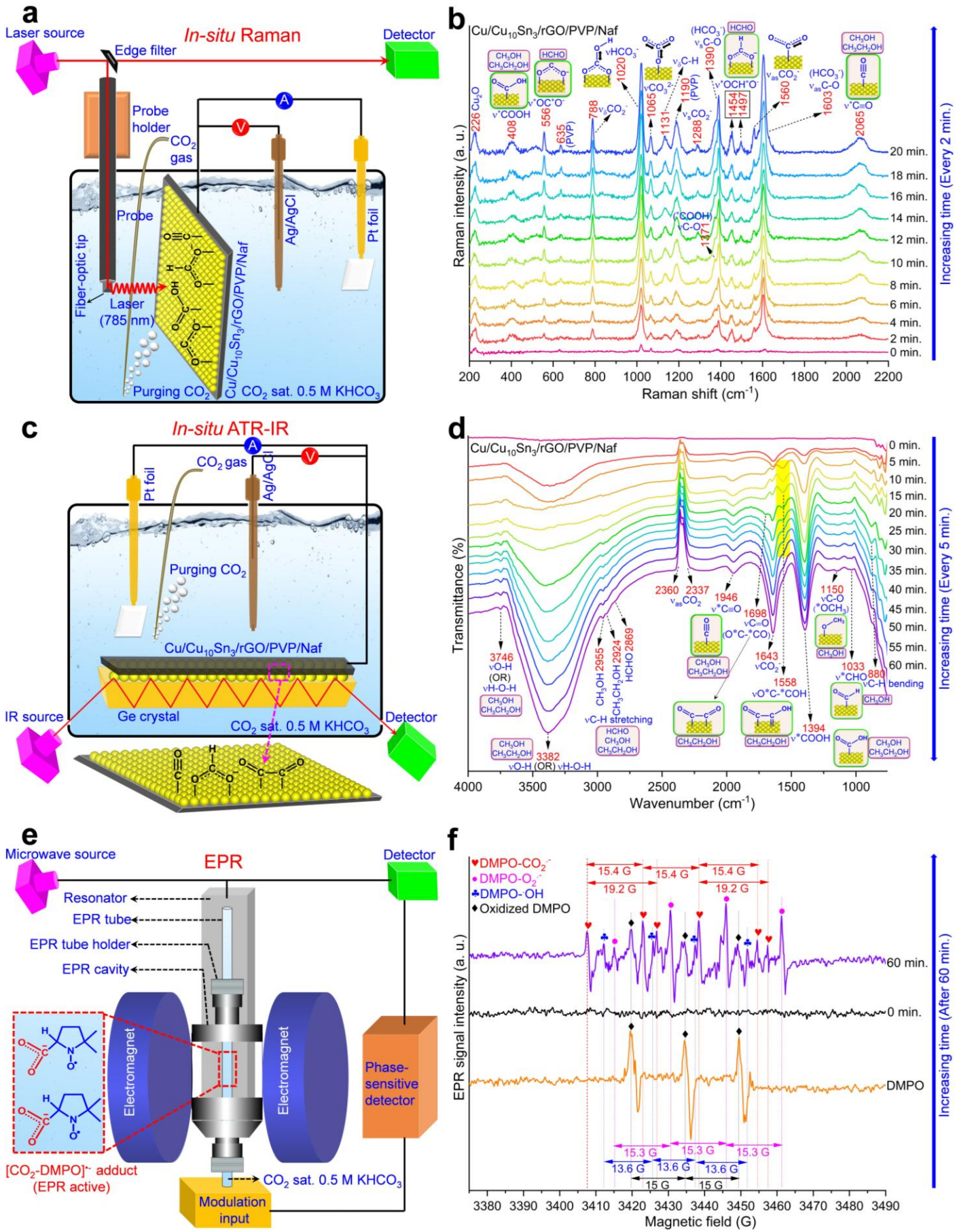
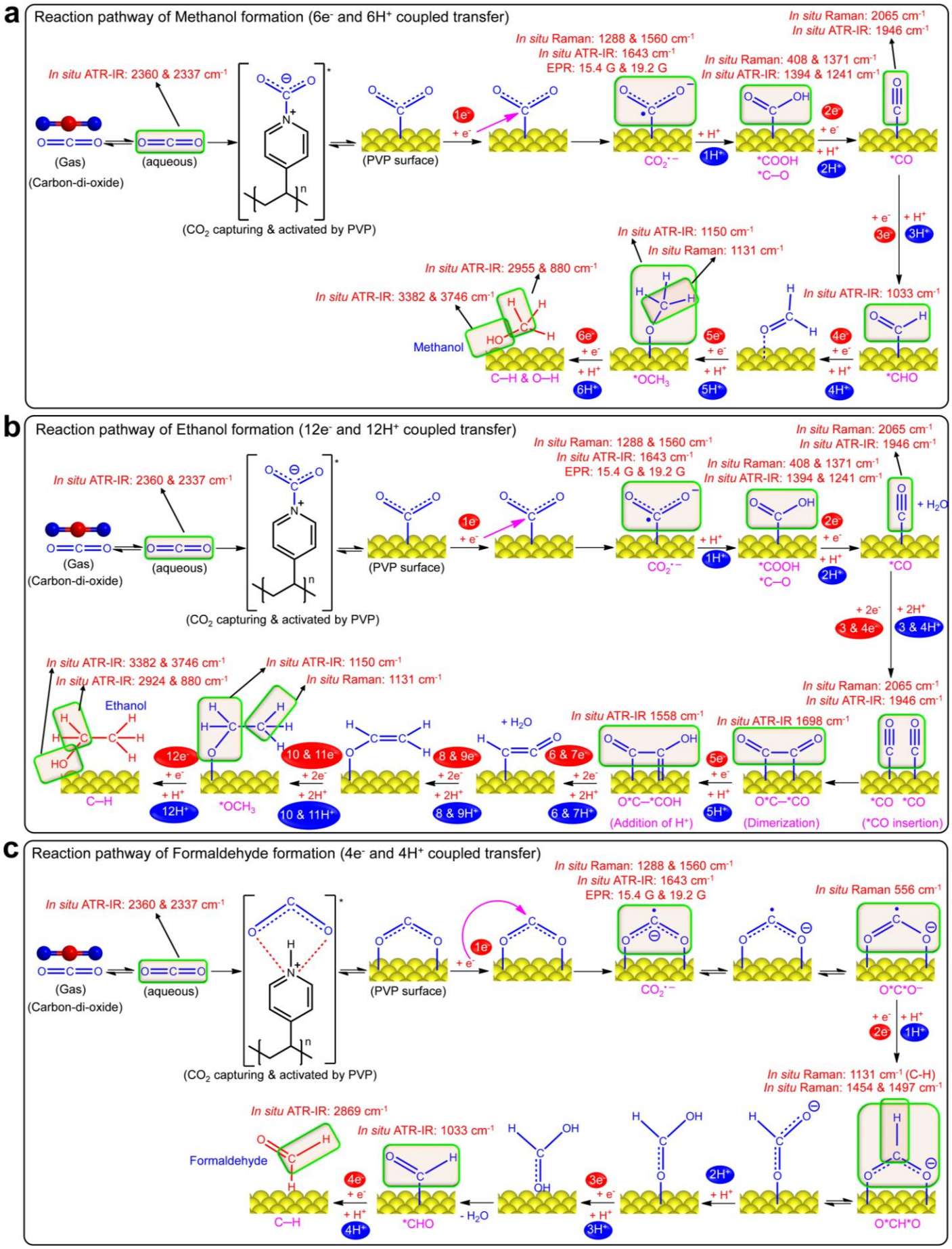

a
Laser source
In-situ Raman
Detector
Edge filter
Probe holder
CO2 gas
Probe
Fiber-optic tip
Laser (785 nm)
Ag/AgCl
Pt foil
Cu/Cu10Sn3/rGO/PVP/Naf
Purging CO2
CO2 sat. 0.5 M KHCO3
b
Cu/Cu10Sn3/rGO/PVP/Naf
Raman intensity (a. u.)
Raman shift (cm-1)
Increasing time (Every 2 min.)
20 min.
18 min.
16 min.
14 min.
12 min.
10 min.
8 min.
6 min.
4 min.
2 min.
0 min.
c
In-situ ATR-IR
CO2 gas
Pt foil
Ag/AgCl
Purging CO2
Cu/Cu10Sn3/rGO/PVP/Naf
IR source
Ge crystal
CO2 sat. 0.5 M KHCO3
Detector
d
Cu/Cu10Sn3/rGO/PVP/Naf
Transmittance (%)
Wavenumber (cm-1)
Increasing time (Every 5 min.)
e
Microwave source
EPR
Detector
Resonator
EPR tube
EPR tube holder
EPR cavity
Electromagnet
Electromagnet
Phase-sensitive detector
[CO2-DMPO]•- adduct (EPR active)
CO2 sat. 0.5 M KHCO3
Modulation input
f
DMPO-CO2-
DMPO-O2•-
DMPO-OH
Oxidized DMPO
15.4 G
19.2 G
EPR signal intensity (a. u.)
60 min.
0 min.
DMPO
15.3 G
13.6 G
15 G
Magnetic field (G)
Increasing time (After 60 min.)

Fig. 5 | *In-situ* spectroscopic investigation of key reaction intermediates and products during CO_2RR over the Cu/$Cu_{10}Sn_3$/rGO/PVP/Nafion MLDC. a, Schematic illustration of the *in-situ* Raman spectroscopy setup, employing a 785 nm laser source with 200 mW output power and custom-designed *in-situ* Raman cell, enabling real-time monitoring of surface-bound intermediates formed during the CO_2RR. **b,** Time-dependent *in-situ* Raman spectra recorded over the Cu/$Cu_{10}Sn_3$/rGO/PVP/Nafion cathode during CO_2RR in CO_2-saturated 0.5 M $KHCO_3$ electrolyte, revealing the progressive formation of key vibrational features. **c**, Schematic representation of the *in-situ* ATR-IR spectroscopy setup, configured with a Ge ATR crystal for enhanced detection of surface-adsorbed species through multiple internal reflections at the electrode/electrolyte interface during CO_2RR. **d,** Time-dependent *in-situ* ATR-IR spectra recorded over the Cu/$Cu_{10}Sn_3$/rGO/PVP/Nafion cathode during CO_2RR in CO_2-saturated 0.5 M $KHCO_3$ electrolyte, revealing the vibrational features of intermediates and products formation. **e,** Schematic of the electron paramagnetic resonance (EPR) setup, designed for low-temperature detection of $CO_2^{\bullet-}$ anion radical intermediates using a DMPO-based spin-trapping strategy. **f**, Time-dependent EPR spectrum collected after 1 hour of CO_2RR reveals six hyperfine splitting signals associated with the DMPO-CO_2 adduct, confirming the formation of the $CO_2^{\bullet-}$ anion radical intermediates.

Proposed reaction pathway and mechanism of PEC CO_2RR - Insights from *in-situ* spectroscopic techniques and DFT calculations

The plausible reaction pathway and underlying mechanism for the formation of methanol, ethanol, and formaldehyde have been proposed based on experimental evidence obtained from *in-situ* Raman*, in-situ* ATR-IR, and EPR spectroscopic techniques along with DFT calculations, as illustrated in Scheme 2a-c. These findings provide compelling evidence for a stepwise multi-electron/multi-proton transfer mechanism operating over the Cu/$Cu_{10}Sn_3$/rGO/PVP/Naf MLDC. The PVP layer on the cathode surface exhibited strong chemisorption affinity toward gaseous CO_2, stabilizing molecules in two different configurations such as $^*CO_2$ or $^*OCO^*$. In the methanol pathway, CO_2 is captured and activated at N-sites of PVP layer, forming a reactive [$PVP^{\delta+}$-$CO_2^{\delta-}$] complex through the transition state of [PVP-$CO_2^{\bullet-*}$]‡ which is the rate-determining step. In the subsequent step, $^*CO_2^{\bullet-}$ is protonated to *COOH and reduced to *C≡O, which then converts *via* *COH → *CHO → *OCH_2 → *OCH_3 to methanol after six electron/proton transfers (Scheme 2a). In the case of ethanol formation pathway, the early-stage intermediates such as $^*CO_2^{\bullet-}$, *COOH, *C≡O remain similar to the methanol formation route. However, ethanol formation proceeds *via* C-C coupling. A second *C≡O is inserted and dimerizes to form a *COCO intermediate. Subsequent proton-electron transfer steps yield *COCOH → *CHCO → *$OCHCH_2$ → *OCH_2CH_3, and ultimately desorbed ethanol after twelve electron/proton steps (Scheme 2b). Four key factors are proposed to account for the efficient formation of ethanol over the

$Cu_{10}Sn_3$/rGO/PVP/Naf MLDC. First, the rGO layer plays a crucial role in accumulating and transferring a high density of electrons owing to its large charge-storage capacity and optimal electronic conductivity. Second, these electrons are subsequently transferred to the PVP interlayer, where CO_2 molecules are substantially captured and activated, resulting in the formation of abundant of *C≡O intermediates. Third, the Nafion overlayer enables rapid proton transport to the CO_2 reduction sites. Forth, the extended lifetime and prolonged surface stabilization of the *C≡O key intermediates ultimately facilitate their dimerization to form *COCO key intermediates, thereby favoring the formation of ethanol product. For formaldehyde formation, CO_2 is adsorbed onto the PVP layer, where both oxygen atoms coordinate with the N-sites of PVP matrix. The first electron transfer forms a $CO_2^{\bullet-}$ intermediate, which rearranges into a surface-bound *OC*O. This species is reduced to *OCH*O and then to *CHO. A fourth electron-proton transfer yields HCHO, which desorbs from the electrode surface (Scheme 2c). These mechanistic insights are supported by *in-situ* Raman, *in-situ* ATR-IR, and EPR spectroscopy along with DFT calculations, and together provide a comprehensive understanding of the electron-proton coupling dynamics leading selective C_1-C_2 solar liquid fuel production.


a
Reaction pathway of Methanol formation (6e⁻ and 6H⁺ coupled transfer)
In situ ATR-IR: 2360 & 2337 cm⁻¹
(Gas)
(aqueous)
(Carbon-di-oxide)
(CO2 capturing & activated by PVP)
(PVP surface)
In situ Raman: 1288 & 1560 cm⁻¹
In situ ATR-IR: 1643 cm⁻¹
EPR: 15.4 G & 19.2 G
CO2•−
In situ Raman: 408 & 1371 cm⁻¹
In situ ATR-IR: 1394 & 1241 cm⁻¹
*COOH
*C—O
In situ Raman: 2065 cm⁻¹
In situ ATR-IR: 1946 cm⁻¹
*CO
In situ ATR-IR: 1033 cm⁻¹
*CHO
In situ ATR-IR: 1150 cm⁻¹
In situ Raman: 1131 cm⁻¹
*OCH3
In situ ATR-IR: 2955 & 880 cm⁻¹
In situ ATR-IR: 3382 & 3746 cm⁻¹
Methanol
C—H & O—H
b
Reaction pathway of Ethanol formation (12e⁻ and 12H⁺ coupled transfer)
In situ ATR-IR: 2360 & 2337 cm⁻¹
(Gas)
(aqueous)
(Carbon-di-oxide)
(CO2 capturing & activated by PVP)
(PVP surface)
In situ Raman: 1288 & 1560 cm⁻¹
In situ ATR-IR: 1643 cm⁻¹
EPR: 15.4 G & 19.2 G
CO2•−
In situ Raman: 408 & 1371 cm⁻¹
In situ ATR-IR: 1394 & 1241 cm⁻¹
*COOH
*C—O
In situ Raman: 2065 cm⁻¹
In situ ATR-IR: 1946 cm⁻¹
*CO
In situ ATR-IR: 3382 & 3746 cm⁻¹
In situ ATR-IR: 2924 & 880 cm⁻¹
Ethanol
C—H
In situ ATR-IR: 1150 cm⁻¹
In situ Raman: 1131 cm⁻¹
*OCH3
In situ ATR-IR 1558 cm⁻¹
O*C—*COH
(Addition of H⁺)
In situ ATR-IR 1698 cm⁻¹
O*C—*CO
(Dimerization)
*CO *CO
(*CO insertion)
c
Reaction pathway of Formaldehyde formation (4e⁻ and 4H⁺ coupled transfer)
In situ ATR-IR: 2360 & 2337 cm⁻¹
(Gas)
(aqueous)
(Carbon-di-oxide)
(CO2 capturing & activated by PVP)
(PVP surface)
In situ Raman: 1288 & 1560 cm⁻¹
In situ ATR-IR: 1643 cm⁻¹
EPR: 15.4 G & 19.2 G
CO2•−
In situ Raman 556 cm⁻¹
O*C*O−
In situ Raman: 1131 cm⁻¹ (C-H)
In situ Raman: 1454 & 1497 cm⁻¹
O*CH*O
In situ ATR-IR: 2869 cm⁻¹
Formaldehyde
C—H
In situ ATR-IR: 1033 cm⁻¹
*CHO

Scheme 2 | Proposed reaction pathways and mechanistic routes for methanol, ethanol, and formaldehyde formation *via* PEC CO_2RR. Schematic illustration of the stepwise PEC CO_2RR over the Cu/$Cu_{10}Sn_3$/rGO/PVP/Nafion MLDC, highlighting the distinct mechanistic routes leading to the selective formation of methanol, ethanol, and formaldehyde. **a**, Methanol formation proceeds *via* a $6e^-/6H^+$ coupled transfer pathway, beginning with the activation of CO_2 at the nitrogen sites of PVP, followed by sequential formation of key intermediates such as *COOH, *CO, *CHO, and *OCH_3. **b**, Ethanol production follows a $12e^-/12H^+$ coupled transfer mechanism, involving initial *CO formation, C-C coupling to form *COCO species, and subsequent reduction of *COCOH, *CHCO, *$OCHCH_2$ and *OCH_2CH_3. **c**, Formaldehyde arises *via* a $4e^-/4H^+$ coupled transfer route, initiated by the reduction of CO_2 to $CO_2^{\bullet-}$, followed by rearrangement to *OCO*, and formation of the bidentate *OCH*O intermediate, further reduced to yield HCHO.

Conclusions

In this work, a highly efficient PEC CO_2RR system was developed by comprising a single-crystalline (040)-facet-engineered $BiVO_4$ photoanode with Cu/$Cu_{10}Sn_3$/rGO/PVP/Naf MLDC. The optimized MLDC architecture, highlighting the functional significance of each layer: the $Cu_{10}Sn_3$ bimetallic alloy facilitates efficient electron transfer from Cu substrate to rGO layer; rGO enables sequential multi-electron transfer to CO_2 reduction sites due to its high charge-storage capacity and optimal electronic conductivity; PVP promotes CO_2 capturing and activation through the formation of a charge-separated [$PVP^{\delta+}$-$CO_2^{\delta-}$] complex; and Nafion ensures rapid and directional proton transport to the CO_2 reduction sites. Collectively, this MLDC architecture, achieved a remarkable Faradaic efficiency of ~91.80% and a record of high solar-to-fuel conversion efficiency of ~1.78%. Comprehensive mechanistic insights into CO_2RR were obtained through *in-situ* Raman, *in-situ* ATR-IR, and EPR spectroscopy, which enabled real-time monitoring of key reaction intermediates and products formation at the electrode/electrolyte interface. Complementary DFT calculations were performed to elucidate the Gibbs free energy changes of key intermediates and products, offering mechanistic insights into the CO_2RR pathways and clarifying the thermodynamics governing the selective formation of methanol, ethanol and formaldehyde. Overall, this work presents a scalable and mechanistically rational approach to PEC CO_2RR, demonstrating the highest STF efficiency reported to date, and offering a promising strategy for advancing solar-driven CO_2 to liquid fuel conversion technologies.

Data availability

The data that supports the findings of this study are available within the article and its Supplementary Information.

References

1. Rahaman, M. *et al.* Solar-driven liquid multi-carbon fuel production using a standalone perovskite-$BiVO_4$ artificial leaf. *Nature Energy* **8**, 629-638, (2023).
2. Bhattacharjee, S. *et al.* Photoelectrochemical CO_2-to-fuel conversion with simultaneous plastic reforming. *Nature Synthesis* **2**, 182-192, (2023).
3. Kim, C. W. *et al.* Artificial Photosynthesis for Formaldehyde Production with 85% of Faradaic Efficiency by Tuning the Reduction Potential. *ACS Catalysis* **8**, 968-974, (2018).
4. Kan, M. *et al.* Defect-Assisted Electron Tunneling for Photoelectrochemical CO_2 Reduction to Ethanol at Low Overpotentials. *Advanced Energy Materials* **12**, 2201134, (2022).
5. Han, G. H. *et al.* Recent Advances in Electrochemical, Photochemical, and Photoelectrochemical Reduction of CO_2 to C_{2+} Products. *Small* **19**, 2205765, (2023).
6. Jung, M. *et al.* Boosting Photoelectrochemical Ethanol Evolution on Reduced Graphene Oxide Functionalized Photocathode. *Advanced Energy Materials* **12**, 2202160, (2022).
7. Ren, D. *et al.* The effects of currents and potentials on the selectivities of copper toward carbon dioxide electroreduction. *Nature Communications* **9**, 925, (2018).
8. Hori, Y. *et al.* Electrochemical Reduction of CO at a Copper Electrode. *The Journal of Physical Chemistry B* **101**, 7075-7081, (1997).
9. Wang, P. *et al.* Phase and structure engineering of copper tin heterostructures for efficient electrochemical carbon dioxide reduction. *Nature Communications* **9**, 4933, (2018).
10. Adit Maark, T. *et al.* CO and CO_2 Electrochemical Reduction to Methane on Cu, Ni, and Cu_3Ni (211) Surfaces. *The Journal of Physical Chemistry C* **120**, 8781-8789, (2016).
11. Zhang, X. *et al.* Atomic nickel cluster decorated defect-rich copper for enhanced C_2 product selectivity in electrocatalytic CO_2 reduction. *Applied Catalysis B: Environmental* **291**, 120030, (2021).
12. Wan, L. *et al.* Bimetallic Cu-Zn Catalysts for Electrochemical CO_2 Reduction: Phase-Separated versus Core-Shell Distribution. *ACS Catalysis* **12**, 2741-2748, (2022).
13. Jeon, H. S. *et al.* Operando Insight into the Correlation between the Structure and Composition of CuZn Nanoparticles and Their Selectivity for the Electrochemical CO_2 Reduction. *Journal of the American Chemical Society* **141**, 19879-19887, (2019).
14. Larrazábal, G. O. *et al.* Microfabricated electrodes unravel the role of interfaces in multicomponent copper-based CO_2 reduction catalysts. *Nature Communications* **9**, 1477, (2018).
15. He, J. *et al.* High-Throughput Synthesis of Mixed-Metal Electrocatalysts for CO_2 Reduction. *Angew. Chem. Int. Ed.* **56**, 6068-6072, (2017).
16. Sarfraz, S. *et al.* Cu-Sn Bimetallic Catalyst for Selective Aqueous Electroreduction of CO_2 to CO. *ACS Catalysis* **6**, 2842-2851, (2016).

17. Gao, J. *et al.* Solar reduction of carbon dioxide on copper-tin electrocatalysts with energy conversion efficiency near 20%. *Nature Communications* **13**, 5898, (2022).
18. Huang, J. *et al.* Structural Sensitivities in Bimetallic Catalysts for Electrochemical CO_2 Reduction Revealed by Ag-Cu Nanodimers. *Journal of the American Chemical Society* **141**, 2490-2499, (2019).
19. Clark, E. L. *et al.* Electrochemical CO_2 Reduction over Compressively Strained CuAg Surface Alloys with Enhanced Multi-Carbon Oxygenate Selectivity. *Journal of the American Chemical Society* **139**, 15848-15857, (2017).
20. Kim, D. *et al.* Synergistic geometric and electronic effects for electrochemical reduction of carbon dioxide using gold-copper bimetallic nanoparticles. *Nature Communications* **5**, 4948, (2014).
21. Tao, Z. *et al.* Copper-Gold Interactions Enhancing Formate Production from Electrochemical CO_2 Reduction. *ACS Catalysis* **9**, 10894-10898, (2019).
22. Ma, S. *et al.* Electroreduction of Carbon Dioxide to Hydrocarbons Using Bimetallic Cu-Pd Catalysts with Different Mixing Patterns. *Journal of the American Chemical Society* **139**, 47-50, (2017).
23. Xie, J.-F. *et al.* Selective electrochemical CO_2 reduction on Cu-Pd heterostructure. *Applied Catalysis B: Environmental* **270**, 118864, (2020).
24. Kang, M. J. *et al.* Selective liquid chemicals on CO_2 reduction by energy level tuned rGO/TiO_2 dark cathode with $BiVO_4$ photoanode. *Applied Catalysis B: Environmental* **295**, 120267, (2021).
25. Kumar, A. *et al.* Highly visible active Ag_2CrO_4/Ag/$BiFeO_3$@RGO nano-junction for photoreduction of CO_2 and photocatalytic removal of ciprofloxacin and bromate ions: The triggering effect of Ag and RGO. *Chemical Engineering Journal* **370**, 148-165, (2019).
26. Park, H. R. *et al.* Enhanced solar photoreduction of CO_2 to liquid fuel over rGO grafted NiO-CeO_2 heterostructure nanocomposite. *Nano Energy* **79**, 105483, (2021).
27. Pawar, A. U. *et al.* General Review on the Components and Parameters of Photoelectrochemical System for CO_2 Reduction with in Situ Analysis. *ACS Sustainable Chemistry & Engineering* **7**, 7431-7455, (2019).
28. Jeong, H. *et al.* Electrochemical CO_2 reduction with low overpotential by a poly(4-vinylpyridine) electrode for application to artificial photosynthesis. *Faraday Discussions* **198**, 409-418, (2017).
29. Barton Cole, E. *et al.* Using a One-Electron Shuttle for the Multielectron Reduction of CO_2 to Methanol: Kinetic, Mechanistic, and Structural Insights. *Journal of the American Chemical Society* **132**, 11539-11551, (2010).
30. Pawar, A. U. *et al.* Crystal facet engineering of ZnO photoanode for the higher water splitting efficiency with proton transferable nafion film. *Nano Energy* **20**, 156-167, (2016).
31. Kang, M. J. *et al.* Selective Alcohol on Dark Cathodes by Photoelectrochemical CO_2 Valorization and Their In Situ Characterization. *ACS Energy Letters* **4**, 1549-1555, (2019).
32. Kim, C. W. *et al.* Energy band edge alignment of anisotropic $BiVO_4$ to drive photoelectrochemical hydrogen evolution. *Materials Today Energy* **13**, 205-213, (2019).
33. Yotsuhashi, S. *et al.* Effect of inserted Si p-n junction on GaN-based photo-electrochemical CO_2 conversion system. *AIP Advances* **4**, 067135, (2014).
34. Deguchi, M. *et al.* Enhanced Capability of Photoelectrochemical CO_2 Conversion System Using an AlGaN/GaN Photoelectrode. *Japanese Journal of Applied Physics* **52**, 08JF07, (2013).

35. Liu, B. *et al.* Back-illuminated photoelectrochemical flow cell for efficient CO_2 reduction. *Nature Communications* **13**, 7111, (2022).
36. Wang, D. *et al. In situ* chloride-mediated synthesis of TiO_2 thin film photoanode with enhanced photoelectrochemical activity for carbamazepine oxidation coupled with simultaneous cathodic H_2 production and CO_2 conversion to fuels. *Journal of Hazardous Materials* **410**, 124563, (2021).
37. Lu, W. *et al.* Reduction of Gas CO_2 to CO with High Selectivity by Ag Nanocube-Based Membrane Cathodes in a Photoelectrochemical System. *Industrial & Engineering Chemistry Research* **59**, 5536−5545, (2020).
38. Irtem, E. *et al.* A photoelectrochemical flow cell design for the efficient CO_2 conversion to fuels. *Electrochimica Acta* **240**, 225-230, (2017).
39. Sekimoto, T. *et al.* Tandem photo-electrode of InGaN with two Si p-n junctions for CO_2 conversion to HCOOH with the efficiency greater than biological photosynthesis. *Applied Physics Letters* **106**, 073902, (2015).
40. Arai, T. *et al.* Solar CO_2 reduction using H_2O by a semiconductor/metal-complex hybrid photocatalyst: enhanced efficiency and demonstration of a wireless system using $SrTiO_3$ photoanodes. *Energy & Environmental Science* **6**, 1274-1282, (2013).
41. Kim, J. *et al.* Robust FeOOH/$BiVO_4$/Cu(In, Ga)Se_2 tandem structure for solar-powered biocatalytic CO_2 reduction. *Journal of Materials Chemistry A* **8**, 8496-8502, (2020).
42. Bian, B. *et al.* Efficient solar-to-acetate conversion from CO_2 through microbial electrosynthesis coupled with stable photoanode. *Applied Energy* **278**, 115684, (2020).
43. Wang, Y. *et al.* Selective CO Production by Photoelectrochemical CO_2 Reduction in an Aqueous Solution with Cobalt-Based Molecular Redox Catalysts. *ACS Applied Materials & Interfaces* **12**, 41644-41648, (2020).
44. Lu, W. *et al.* Efficient Photoelectrochemical Reduction of Carbon Dioxide to Formic Acid: A Functionalized Ionic Liquid as an Absorbent and Electrolyte. *Angew. Chem. Int. Ed.* **56**, 11851-11854, (2017).
45. Rudolph, W. W., Irmer, G. & Königsberger, E. Speciation studies in aqueous HCO_3^--CO_3^{2-} solutions. A combined Raman spectroscopic and thermodynamic study. *Dalton Transactions*, 900-908, (2008).
46. Shan, W. *et al.* In Situ Surface-Enhanced Raman Spectroscopic Evidence on the Origin of Selectivity in CO2 Electrocatalytic Reduction. *ACS Nano* **14**, 11363-11372, (2020).
47. Jiang, S., Klingan, K., Pasquini, C. & Dau, H. New aspects of operando Raman spectroscopy applied to electrochemical CO2 reduction on Cu foams. *The Journal of Chemical Physics* **150**, (2018).
48. Zhang, J. *et al.* Accelerating electrochemical CO2 reduction to multi-carbon products via asymmetric intermediate binding at confined nanointerfaces. *Nature Communications* **14**, 1298, (2023).
49. Bohra, D. *et al.* Lateral Adsorbate Interactions Inhibit $HCOO^-$ while Promoting CO Selectivity for CO2 Electrocatalysis on Silver. **58**, 1345-1349, (2019).
50. Liu, P. *et al.* Synergy between Palladium Single Atoms and Nanoparticles via Hydrogen Spillover for Enhancing CO2 Photoreduction to CH4. **34**, 2200057, (2022).
51. Kim, Y. *et al.* Time-resolved observation of C–C coupling intermediates on Cu electrodes for selective electrochemical CO2 reduction. *Energy & Environmental Science* **13**, 4301-4311, (2020).

52. Li, X. *et al.* Selective visible-light-driven photocatalytic CO2 reduction to CH4 mediated by atomically thin CuIn5S8 layers. *Nature Energy* **4**, 690-699, (2019).
53. Qiu, X.-F., Zhu, H.-L., Huang, J.-R., Liao, P.-Q. & Chen, X.-M. Highly Selective CO2 Electroreduction to C2H4 Using a Metal–Organic Framework with Dual Active Sites. *Journal of the American Chemical Society* **143**, 7242-7246, (2021).
54. Alsalka, Y., Al-Madanat, O., Curti, M., Hakki, A. & Bahnemann, D. W. Photocatalytic H2 Evolution from Oxalic Acid: Effect of Cocatalysts and Carbon Dioxide Radical Anion on the Surface Charge Transfer Mechanisms. *ACS Applied Energy Materials* **3**, 6678-6691, (2020).
55. Li, L. *et al.* Evolution of bismuth-based metal–organic frameworks for efficient electroreduction of CO2. *Journal of Materials Chemistry A* **10**, 17801-17807, (2022).
56. Li, R. *et al.* Carbon Dioxide Anion Radicals Assisted Highly Efficient Photocatalytic H2O2 Production over Bi(C2O4)OH. *The Journal of Physical Chemistry Letters* **14**, 10570-10577, (2023).
57. Villamena, F. A., Locigno, E. J., Rockenbauer, A., Hadad, C. M. & Zweier, J. L. Theoretical and Experimental Studies of the Spin Trapping of Inorganic Radicals by 5,5-Dimethyl-1-Pyrroline N-Oxide (DMPO). 1. Carbon Dioxide Radical Anion. *The Journal of Physical Chemistry A* **110**, 13253-13258, (2006).
58. Wang, T. *et al.* Engineering Catalytic Interfaces in Cuδ+/CeO2-TiO2 Photocatalysts for Synergistically Boosting CO2 Reduction to Ethylene. *ACS Nano* **16**, 2306-2318, (2022).

Acknowledgements

This work was financially supported by Korea Evaluation Institute of Industrial Technology (Alchemist Project 20018904, NTIS-141518011) through the Ministry of Trade, Industry and Energy, Korea. This research work is also supported by the Regional Leading Research Center Program (2019R1A5A8080326). The author, S. Prabhakaran, would also like to express sincere gratitude to Dr. Hyunseok Ko of the Korea Institute of Ceramic Engineering and Technology (KICET) for kindly providing the space and facilities to perform post-work calculations related to DFT. The authors wish to thank Dr. Weon-Sik Chae of Korea Basic Science Institute (KBSI) Daegu Center for the TR-PL measurements.

Author contributions

R.P.S. and Y.S.K. conceived and designed the experiments. R.P.S. synthesized the bimetallic alloy catalysts and rGO, fabricated the multi-layer dark cathode, carried out material characterization, assembled the device, and performed all PEC CO_2RR experiments as well as the *in-situ* spectroscopic studies. S.R.P.S. fabricated the (040)-faceted $BiVO_4$ photoanode. A.U.P., L.Y., and D.K.L. designed and optimized the PEC CO_2RR setup. S.P. performed the DFT calculations under the supervision of D.H.K. K.M.P. and M.S.K.

analyzed the liquid and gaseous products using gas chromatography. S.Y. and Y.S.-H. critically reviewed and revised the whole manuscript. H.H. critically reviewed and revised the whole manuscript. H.S. provided research funding. Y.S.K. supervised the overall project. All authors discussed the results and contributed to the final manuscript.

Declaration of Competing Interest

The authors declare that they have no competing financial interests or personal relationships that could have influenced the work reported in this paper.

Additional information

Supplementary information file is available.

Supplementary Files

This is a list of supplementary files associated with this preprint. Click to download.

- YoungSooKangNat.Chem.SupplementaryinformationPECCO2RR20251216.docx
- RevisedYoungSooKangNat.Chem.SupplementaryinformationPECCO2RR20251224.docx